Reconstructing atmospheric H_2 over the past century from bi-polar firn air records

John D. Patterson[1], Murat Aydin[1], Andrew M. Crotwell[2,3], Gabrielle Pétron[2,3], Jeffery P. Severinghaus[4], Paul B. Krummel[5], Ray L. Langenfelds[5], Vasilii V. Petrenko[6], and Eric S. Saltzman[1]

[1]Department of Earth System Science and Chemistry, University of California, Irvine, Irvine, CA 92697, USA
[2]Cooperative Institute for Research in Environmental Sciences, University of Colorado Boulder, Boulder, CO 80309, USA
[3]Global Monitoring Laboratory, National Oceanic and Atmospheric Administration, Boulder, CO 80305, USA
[4]Scripps Institution of Oceanography, University of California, San Diego, La Jolla, CA 92093, USA
[5]Climate Science Centre, Commonwealth Scientific and Industrial Research Organisation, Environment, Aspendale, Victoria 3195, Australia
[6]Department of Earth and Environmental Sciences, University of Rochester, Rochester, NY 14627, USA

Correspondence to: John D. Patterson (jdpatter@uci.edu)

Abstract

Historical hemispheric atmospheric H_2 levels since 1930 were reconstructed using the UCI_2 firn air model and firn air measurements from three sites in Greenland: (NEEM, Summit, and Tunu) and two sites in Antarctica (South Pole and Megadunes). A joint reconstruction based on the two Antarctic sites yields H_2 levels monotonically increasing from about 350 ppb in 1900 to 550 ppb in the late 1990's, levelling off thereafter. These results are similar to individual reconstructions published previously (Patterson et al., 2020; 2021). Reconstruction of the Greenland data is complicated by a systematic bias between Tunu and the other sites. The Tunu reconstruction shows substantially lower historical H_2 levels than the other two sites, a difference we attribute to possible bias in the calibration of the Tunu measurements. All three reconstructions show a late 20th century maximum in H_2 levels over Greenland. A joint reconstruction of the Greenland data shows H_2 levels rising 40% from 1930-1990, reaching a maximum of 550 ppb. After 1990, reconstructed atmospheric H_2 decrease by 6% over the next 20 years. The reconstruction deviates by at most 4% from the few available surface air measurements of atmospheric H_2 levels over Greenland from 1998-2004. However, the longer instrumental records from sampling sites outside of Greenland show a more rapid decrease and stabilization after 1990 compared to the reconstruction. We explore the possibility that this difference is an artefact caused by the firn air model underestimating pore close-off induced enrichment, evidenced by a mismatch between measured and modelled Ne in firn air. We developed new parameterizations which more accurately capture pore close-off induced enrichment at the Greenland sites. Incorporating those parameterizations into the UCI_2 model yields reconstructions with lower H_2 levels throughout the mid-late 20th century and more stable H_2 levels during the 1990's, in better agreement with the flask measurements.

1 Introduction

Molecular hydrogen (H_2) is the second-most abundant reduced gas in Earth's atmosphere after methane. Atmospheric H_2 levels are linked to Earth's radiative budget, air quality, and the atmospheric oxidative capacity (eg. Ehhalt & Rohrer, 2009; Novelli et al., 1999; Paulot et al., 2021). As H_2 becomes a more important component of the energy sector, anthropogenic emissions of H_2 are expected to rise substantially (Derwent et al., 2020; Prather, 2003; Wang et al., 2013a, 2013b). Projecting the atmospheric response to increased anthropogenic emissions in a changing climate requires a comprehensive understanding of the biogeochemical cycle of H_2. Studying past changes in atmospheric H_2 can inform predictions of the effects of future perturbations by providing insight into the relationship between atmospheric H_2, human activities, and climate.

The globally averaged mixing ratio of H_2 in the present-day atmosphere is roughly 530 nmol mol^{-1} (ppb; Pétron et al., 2023). Major sources of atmospheric H_2 include direct emissions from fossil fuel combustion and biomass burning and photochemical production from the oxidation of methane and non-methane hydrocarbons (NMHCs). Direct emission as a by-product of N_2 fixation is a minor source of atmospheric H_2. The major sink of atmospheric H_2 is consumption by soil microbes, accounting for about 70% of total losses and the remainder of the losses are to oxidation by the OH radical. Based on the atmospheric burden and estimates of the microbial and OH sinks, the lifetime of H_2 is estimated at 2 years (Novelli et al., 1999; Pieterse et al., 2011; 2013; Paulot et al., 2021).

Increasing atmospheric H_2 could influence the climate system in several ways. The reaction of H_2 with OH represents a loss for OH and therefore increases the atmospheric methane lifetime and associated radiative forcing. This reaction leads to the production of HO_2, which can influence tropospheric ozone levels. In the stratosphere, the reaction of H_2 with OH leads to the production of water vapor. Increased stratospheric water vapor cools the stratosphere and warms the troposphere (Solomon et al., 2010). Paulot et al. (2021) estimated the effective radiative forcing of atmospheric H_2 at 0.13 mW m^{-2} ppb^{-1} due to its effects on the methane lifetime and stratospheric water vapor content.

Systematic measurements of atmospheric H_2 levels began in the late 1980's (Khalil & Rasmussen, 1990). The NOAA Global Monitoring Laboratory (NOAA/GML), CSIRO GASLAB (CSIRO), and the Advanced Global Atmospheric Gases Experiment (AGAGE) started to monitor atmospheric H_2 levels at several sites around the world in the early 1990's (Novelli et al., 1999; Novelli, 2006; Prinn et al., 2019; Langenfelds et al., 2002; Pétron et al., 2023). Integration of records produced by the different groups has been complicated by calibration issues, which are discussed in greater detail in Section 5. Earlier use of different scales was addressed by implementation of the internationally accepted MPI09 scale established by the Max Planck Institute for Biogeochemistry (MPI; Jordan & Steinberg, 2011). Measurements from CSIRO and AGAGE, have been transferred to the MPI09 scale. Additionally, NOAA/GML measurements from 2009 onward were recently revised to the MPI09 scale (Pétron et al., 2023). Broadly, the instrumental record shows northern hemispheric H_2 levels rising during the late 1980's to a maximum in 1990 and decreasing until 1993. There is no discernible trend in Northern Hemisphere H_2 levels from 1993-2010 (Figure 3). The Southern Hemisphere instrumental record shows H_2 levels rising until 1999, then plateauing for the next 10-15 years.

2

Longer-term changes in atmospheric H_2 levels during the 20th century have been reconstructed using polar firn air from Antarctica (South Pole, Megadunes) and Greenland (NEEM; Petrenko et al., 2013; Patterson et al., 2020; 2021). Firn is the compacted snow layer that forms the upper $40 - 120$ m of ice sheets and its interconnected porosity contains an atmospheric archive (referred to as "firn air) that can extend up to $\approx$100 years back in time. For a comprehensive introduction to firn and firn air we refer the interested reader to Buizert (2013). The Antarctic reconstructions show that H_2 levels increased by 60% over the 20th century, consistent with the instrumental record and with increasing anthropogenic emissions and photochemical production from methane (Patterson et al., 2020). The Greenland reconstruction shows an increase in atmospheric H_2 levels during the 1960's to a peak in the late 1980's or early 1990's, followed by a small decline from 1990-2009 (Petrenko et al., 2013). This recent decline is inconsistent with northern hemisphere modern flask measurements that show roughly constant H_2 levels after the mid-1990's (Novelli, 2006; Prinn et al., 2019). Petrenko et al. (2013) noted that the firn air model used for that reconstruction did not include pore close-off fractionation, a process that enriches H_2 in the lock-in zone where vertical diffusion of trace gases effectively goes to zero. Patterson et al. (2020) suggested that the inferred peak could be an artifact of ignoring this process.

In this work, we reassess historical Northern Hemisphere atmospheric H_2 levels over the 20th century using firn air from NEEM and two additional Greenland sites with previously unpublished H_2 measurements (Summit and Tunu). Additionally, we reanalyse the Antarctic firn air data using a different inversion technique, described in Section 3.2. Reliable bipolar records are useful for constraining changes to H_2 cycling because the two hemispheres differ in their sensitivity to changes in the soil sink and anthropogenic emissions. Understanding past variability in the soil sink is particularly important because the response of the soil sink to future changes in climate is the largest source of uncertainty in projecting the radiative consequences of increasing anthropogenic H_2 emissions (Warwick et al., 2022).

2. H$_2$ measurements in Greenland firn air

2.1 Firn air sampling

The sampling methods used in the Summit, Tunu, and NEEM campaigns were similar to techniques from previous published firn air studies (e.g. Battle et al., 1996; Severinghaus et al., 2001; Severinghaus & Battle, 2006). Briefly, a borehole was drilled into the firn, pausing the drilling at each desired sampling depth. The borehole was sealed above each sampling depth with an inflatable rubber packer to prevent contamination from the modern atmosphere. Synflex 1300 (formerly known as "Decabon") tubing for both waste air and sample air extends from below the packer to the surface. The waste air intake was positioned directly below the rubber packer. The waste air intake was separated from the sample air intake by a stainless-steel plate (baffle) with a diameter slightly less than the borehole. Air was pumped from the waste air intake 2-5x faster than from the sample air intake to ensure that no air that had been in contact with the rubber packer was sampled. Sampled air was dried

using Mg(ClO$_4$)$_2$ and stored in 2.5 L glass flasks. More detailed information regarding the sampling at each site may be found in the references listed in Table 1.

Table 1- Site characteristics and data references for the three Greenland firn air sampling campaigns.

Site	Lat/lon	Date	T (°C)[1,4]	Accum.[2,4]	Reference	Firn air model parameters[3,5]
NEEM	77°N, 51°W	7/2008	-29	21.6	Petrenko et al., 2013	Buizert et al., 2012
Summit	73°N, 38°W	5/2013	-31	23.4	Hmiel et al., 2020	C. Buizert, personal communication
Tunu	78° N, 34° W	5/1996	-29	10.0	Butler et al., 1999	This study

[1]Mean annual surface temperature
[2]Average modern accumulation (cm ice equivalent per year)
[3]Modeling parameters include density profile, diffusivity profile, and the lock-in depth (Section 3.1).
[4]Temperature and accumulation for NEEM and Tunu are from Buizert et al. (2012) and Butler et al. (1999) respectively. Temperature and accumulation for Summit were supplied by Christo Buizert (Personal Communication).
[5]Partitioning between closed and open porosity is based on Schwander (1989) for all three sites.

2.2 Firn air measurements and calibration

Firn air samples from Tunu were analyzed for H$_2$ by the NOAA/GML Carbon Cycle Group using a reducing gas analyzer (RGA) with HgO detection (Novelli et al., 1999). At the time of analysis, the measurements were calibrated using a single 530 ppb H$_2$ standard assuming a linear detector response. We subsequently applied an empirical correction to account for the non-linear response of the HgO-RGA. The non-linearity bias is estimated to be -3 ppb at 453 ppb and -12 ppb at 312 ppb based on laboratory measurements made at NOAA/GML in 2009. The biases were linearly interpolated onto the firn air measurements (i.e. a measurement of 300 ppb was corrected to 312 ppb; Patterson et al., 2021). Jordan & Steinberg (2011) found a substantially larger non-linearity bias for a similar RGA detector. The sensitivity of our results to uncertainty in the non-linearity correction is minimal as demonstrated in the Supplement (Figures S3 and S4). The Tunu data were originally calibrated on the NOAA96 H$_2$ calibration scale, that is known to have drifted due to H$_2$ increasing in the GML gravimetric standards stored in aluminum cylinders. We adjusted the Tunu firn air measurements to the MPI09 scale based on a matched flask intercomparison between NOAA/GML and CSIRO conducted using atmospheric samples from the Cape Grim Observatory, Tasmania during June and July 1996. The intercomparison gives an average offset (CSIRO-NOAA/GML) of 4.7 ppb. A constant correction of 4.7 ppb was added to the Tunu measurements to account for the offset. The Summit firn air measurements were made by NOAA/GML using a He pulsed discharge detector with linear response (HePDD; Novelli et al., 2009). The Summit measurements have been formally revised to the MPI09 calibration scale. For both the Tunu and Summit data, the corrections described above are below 5% and do not significantly influence the main conclusions of this research.

Firn air samples from NEEM were analyzed for H$_2$ at CSIRO using gas chromatography coupled to an HgO-RGA. These measurements were calibrated using standards between 340 and 1000 ppb. The CSIRO measurements have been revised

4

to the MPI09 scale. CSIRO estimates the analytical uncertainty to be ±0.2%. However, there are other sources of uncertainty in the true H_2 content in the firn air. For example, tests conducted during the NEEM campaign demonstrated a small procedural blank (4-6 ppb). No such tests were conducted at the other sites. To account for the possibility of such blanks, we assign an overall uncertainty of ±2% to the data from all sites.

130   The firn air H_2 measurements from all three sites were corrected for gravitational fractionation (equation 2; Section 3.1), and duplicate measurements at the same depth were averaged to generate the finalized depth profiles (Figure 1b-d; 2b-d). Lock-in depths for the sites are given in Table 2. The H_2 depth profiles at the three Greenland sites display strong gradients above lock-in that reflect the fast free air diffusivity of H_2 and intense seasonality of atmospheric H_2 in the northern hemisphere. The H_2 gradients observed in the upper firn at NEEM are different than the gradients at Summit and Tunu because NEEM was

135   sampled in July while the other two sites were sampled in May. The depth profiles from NEEM and Summit both display sharp maxima of 530 and 560 ppb respectively in the lock-in zone. In contrast, Tunu H_2 levels do not display a peak in the lock-in zone. Instead, the Tunu H_2 measurements are approximately constant for the 10 m just above lock-in and then decrease significantly to a minimum of 420 ppb at the bottom of lock-in. The NEEM measurements also show a sharp decrease to 490 ppb at the bottom of lock-in. At Summit, the decrease towards the bottom of lock-in is less dramatic than at the other sites

140   because only one sample depth is deeper than the observed maximum. The qualitative differences in the depth profiles reflect changes in surface air H_2 levels over the period of the firn air studies (1996-2013) and the different physical characteristics of the sites. For example, the firn air at the bottom of the lock-in zone at Summit is younger than the two other sites because: 1) Summit was sampled later than the other sites and 2) Summit has a much higher accumulation rate than Tunu and a thinner lock-in zone than NEEM (Table 1).

145

Table 2- Summary of firn air H_2 measurements from NEEM, Summit, and Tunu.

Site	Samples	Unique Depths	Lab	Detector	Lock-in depth (m)
NEEM	23	18	CSIRO	HgO-RGA	63
Summit	37	19	NOAA	HePDD	68.5
Tunu	48	22	NOAA	HgO-RGA	58

3. Firn air modelling and inversions

3.1 Firn air model

The UCI_2 firn air model is a 1-dimensional finite-difference advective-diffusive model that is used to simulate the

150   evolution of trace gas levels in firn air. The UCI_2 model has been used to successfully analyse H_2 levels in firn air at two Antarctic sites, including the effects of pore close-off fractionation (see below; Patterson et al., 2020; 2021). As discussed in

Section 7, the default model parameterizations do not adequately capture the effects of pore close-off fractionation at two of the Greenland sites; nonetheless, the model provides a useful baseline for analysing atmospheric H_2 levels in firn air.

155   The UCI_2 model is largely based on Severinghaus et al. (2010). The model domain is divided into an upper "diffusive zone" and lower "lock-in zone." In the diffusive zone, vertical gas transport occurs via wind-driven mixing in the shallowest ~5 m and via molecular diffusion throughout. Diffusive mixing decreases with depth due to the increasing tortuosity of the firn. In the lock-in zone, vertical molecular diffusion ceases due to the presence of impermeable ice layers. Gas transport in the lock-in zone occurs primarily due to advection with a small non-fractionating mixing term. The model uses a forward Euler integration scheme and a time step of 324 s., There are three important differences between the Severinghaus et al. (2010)

160   model and the UCI_2 model: 1) thermal diffusion is neglected, as it is unimportant for H_2, 2) backflow due to densification in the lock-in zone is neglected in order to yield a better empirical fit to the tuning gases, and 2) our model parameterizes pore close-off fractionation differently than the Severinghaus model (see below). The model tracks the air content and composition in both open pores and closed bubbles as a function of time and depth. The model code is written and executed in MATLAB R2022a (Mathworks Inc.).

165   The site-specific bulk density profile (ρ_{firn}: kg m^{-3}) is calculated from an empirical fit to density measurements of the firn core. Total porosity (s_{total}; dimensionless) is estimated from the density profile:

$$s_{total} = 1 - \frac{\rho_{firn}}{\rho_{ice}} \tag{1}$$

170   Where ρ_{ice} (kg m^{-3}) is the temperature dependent density of ice from Bader (1964). Accumulation rate, temperature, and the depth of the lock-in zone onset are site-specific parameters, and we implement previously published parameterizations for the partitioning between open and closed porosity at each site (Tables 1 and 2, Schwander, 1989).

Model grid spacing is 0.5 m in the diffusive zone. Gas transport is dominated by wind-driven mixing in the upper part of the diffusive zone, and by molecular diffusion in the lower part of the diffusive zone. To simulate non-fractionating

175   wind-driven mixing, a depth-dependent eddy diffusivity term is added to the one-dimensional firn air transport equation (Schwander et al., 1993; Severinghaus et al., 2010; Trudinger et al., 1997). Additionally, we neglect the typical gravitational term, and instead empirically correct the firn air measurements using the $\delta^{15}N$ of N_2 depth profile. The correction is calculated from the $\delta^{15}N$ data for each borehole according to equation 2:

180     $$Corr_{grav} = \frac{\delta^{15}N}{1000} * \frac{\exp\left(g*z*\frac{\Delta m g}{RT}\right)-1}{\exp\left(g*z*\frac{\Delta m_{15}}{RT}\right)-1} \tag{2}$$

Where $Corr_{grav}$ is the depth dependent fractional correction for the gas of interest, $\delta^{15}N$ is the measured isotopic composition of N_2 (‰) each depth, g is the gravitational acceleration constant (9.8 m s^{-2}), z is depth (m), R is the ideal gas constant (8.314

J mol^{-1} K^{-1}), T is the annual average temperature at the site, Δm_g is the difference in molar mass (in kg) between the gas of interest and air, and Δm_{15N} is the difference in molar mass between $^{28}N_2$ and $^{29}N_2$ (.001 kg). This correction neglects the thermal fractionation of $\delta^{15}N$. Thermal fractionation is only important in the upper ~20 m of the firn, and these shallow measurements are excluded from the reconstructions due to seasonality (Severinghaus et al., 2001; Section 3.2).

Equation 3 governs the evolution of the concentration of the gas of interest in the open pores in the diffusive zone (Severinghaus et al., 2010):

$$s_o \frac{\partial c}{\partial t} = \frac{\partial}{\partial z}\left(\frac{\partial c}{\partial z} * \left[s_o D_{mol}(z,T,P) + s_o D_{eddy}(z)\right]\right) - s_o w \frac{\partial c}{\partial z} \tag{3}$$

Where s_o is the open porosity, C is concentration of the gas of interest (mol m^{-3}), D_{mol} is the gas, depth, temperature, and pressure dependent molecular diffusivity constant (m^2 s^{-1}), D_{eddy} is the depth dependent eddy diffusivity (m^2 s^{-1}), and w is the downward velocity of the firn column (m s^{-1}). We used D_{mol} and D_{eddy} profiles for NEEM and Summit developed previously using a suite of measured gases with well constrained atmospheric histories of CO_2, CH_4, CH_3CCl_3, and SF_6 (Buizert et al., 2012; Hmiel et al., 2020; C. Buizert, personal communication). The diffusivity profiles were validated by forcing the model with the established atmospheric histories for the previously mentioned trace gases and comparing the model output to the measurements. Diffusivity profiles for Tunu were tuned using CO_2 and CH_4 measurements. During the tuning process, the ratio between the effective molecular diffusivities of each trace gas at each depth is forced to remain identical to the ratio of their free air diffusivities (i.e. at each depth D_{mol} for CH_4 is 1.4 time that of D_{mol} for CO_2). After tuning D_{mol} is then scaled using the ratio of the free air diffusivity of CO_2 to the diffusivity of H_2 or other trace gas of interest. Temperature and pressure dependent free air diffusivities are calculated using Fuller et al. (1966) as described by Reid et al. (1987; Ch. 11).

Model grid spacing in the lock-in zone is 1 annual layer. There is no molecular diffusivity in the lock-in zone and gas transport occurs via downward advection of annual layers once per year. At the top of lock-in, small, non-fractionating values of "eddy diffusivity" are prescribed to account for dispersive mixing caused by barometric pressure fluctuations (Buizert and Severinghaus, 2016). Model parameterizations for vertical mixing in the lock-in zone are validated by forcing the model with best-estimate Greenland atmospheric histories for various trace gases with well constrained atmospheric histories (Buizert et al., 2012).

In addition to wind-driven mixing, diffusion and advection, pore close-off fractionation is parameterized in the firn air model. As closed pores (bubbles) are advected downward in the firn, internal pressure increases, creating a partial pressure gradient which drives a net diffusive flux of highly mobile trace gases out of the bubbles, through the ice lattice, and into the open pores. The open pores are therefore enriched in these gases. This phenomenon affects gases with kinetic diameters (KD) <3.6 Å such as Ne, and He due to their large diffusivity in ice (Severinghaus & Battle, 2006).

Given its small molecular diameter (KD= 2.89 Å) pore close-off fractionation must affect H_2 in a similar manner to Ne (Patterson et al., 2020; Petrenko et al., 2013, Severinghaus & Battle, 2006). Recent laboratory measurements indicate that

the permeability of H_2 in ice is sufficiently fast to equalize the partial pressure of H_2 in the open porosity and closed bubbles (Patterson & Saltzman, 2021). Therefore, in the model, it is assumed that the partial pressure of H_2 is in equilibrium between the closed bubbles and open pores in each layer as described by equations 4-6:

220

$$P_n = (P_{bubble} x_{n(bubble)} s_c + P_{ambient} x_{n(firn)} s_o)/s_{total} \tag{4}$$

$$x_{n(bubble)} = P_n/P_{bubble} \tag{5}$$

225 $\quad x_{n(firn)} = P_n/P_{ambient} \tag{6}$

Where P_n (Pa) is partial pressure of gas n (H_2 or Ne; See section 5), x_n is mole fraction of gas n, P_{bubble} (Pa) is the total bubble pressure, $P_{ambient}$ (Pa) is the ambient pressure in the open pores, and s_c is closed porosity. The subscripts *bubble* and *firn* distinguish between the closed and open porosity. Equations 4-6 are executed at every time step in each grid cell in the model.

230 Note that the equilibrium parameterization of pore close-off fractionation used here is different from the kinetic parameterization used by Severinghaus & Battle (2006) which was developed assuming a much smaller permeation constant for Ne. Pore close-off fractionation is important in terms of the exchange of H_2 and Ne between closed and open pores. Permeation of these gases through the ice lattice vertically between model layers can be neglected on time scales relevant to firn air modelling (Patterson & Saltzman 2021).

235

3.2 Inversion methods

The firn air measurements are inverted to recover an atmospheric history of H_2 from each site. The inversion technique employs depth-dependent age distributions or "Green's functions" (*G;* Rommelaere et al., 1997). The firn air model is initialized with no H_2 in the firn air column, then forced with a transient 1-year pulse of H_2 at the surface. The model is

240 integrated for 300 years, and the evolution of the pulse is tracked as a function of depth and time to produce the Green's functions. The age distributions grow older and broader with depth (Figure S1). For most gases, the Green's functions sum to 1 at every depth. In the case of H_2 and Ne, the sum of the Green's functions in the lock-in zone is >1 due to pore close-off fractionation. Given an atmospheric history ($H_{2(atm)}$), modelled levels of H_2 in the firn ($H_{2(firn)}$) are calculated according to equation 7:

245

$$H_{2(firn)}(z) = \sum_{t=0}^{300} H_{2(atm)}(t) * G(z,t) \tag{7}$$

Using Green's function allows for rapid iteration over many possible atmospheric histories without running the firn air model in forward mode. The inversion problem is under-constrained. Multiple atmospheric histories can provide good agreement with the measured depth profile, and additional constraints are required to yield a unique solution. In previous studies, the additional constraint has been implemented as a smoothing parameter (Patterson et al., 2020, 2021; Petrenko et al., 2013; Rommelaere et al., 1997). In this work, we rely instead on the assumption of autocorrelation and utilize the probabilistic modelling software package, Stan (mcstan.org). Stan has been used previously for firn air reconstructions by Aydin et al. (2020). As in that work, we use Stan to implement a Bayesian hierarchical model in which the atmospheric history is treated as an auto-correlated random variable:

$$\boldsymbol{m_{atm}}[t_i] \sim N(\boldsymbol{m_{atm}}[t_{i-1}], \beta \, \boldsymbol{m_{atm}}[t_{i-1}]) \tag{8}$$

Where N is the normal distribution, and $\boldsymbol{m_{atm}}$ is a vector of length i that contains the discrete atmospheric H_2 dry air mole fraction history with a timestep of 1 year. The atmospheric mixing ratio at time t_i is normally distributed around the atmospheric mixing ratio at time t_{i-1} with a standard deviation of $\beta \, \boldsymbol{m_{atm}}[t_{i-1}]$. β is a positive scalar which may be specified or varied as a free parameter. The atmospheric history is related to the firn air measurements:

$$\boldsymbol{h_{obs}} \sim N(\boldsymbol{G m_{atm}}, \boldsymbol{\sigma}) \tag{9}$$

Where $\boldsymbol{h_{obs}}$ is a vector of length n, which contains the measured H_2 levels at each depth, $\boldsymbol{G}$ is an n by i matrix where each row corresponds to the Green's function for that unique depth (referred to as the "kernels" by Rommeleaere et al. (1997)), and $\boldsymbol{\sigma}$ is a vector of length n, which contains the analytical uncertainties of the firn air measurements. Stan samples the joint posterior probability distribution for the parameters, $\boldsymbol{m_{atm}}$ and β using a fast Hamiltonian Markov Chain Monte Carlo algorithm (Carpenter et al., 2017). Parameters are sampled from uniform prior distributions unless otherwise specified. Inversions are carried out using the MatlabStan 2.15.1.0 interface to cmdstan 2.27.0. The advantages of this method over other methods include: 1) No arbitrarily specified smoothing criteria is imposed (instead the atmospheric history is assumed to be autocorrelated), and 2) Stan allows us to easily explore sensitivity to assumptions about the data by encoding those assumptions as priors.

In Greenland, H_2 levels in the upper firn layers are strongly influenced by seasonal variations, and firn air reconstructions cannot accurately reconstruct such high frequency variability. Therefore, measurements from the upper part of the firn were excluded from the reconstructions. A cut-off depth was determined by forcing the firn air model in forward mode with an atmospheric history that consisted of constant annually averaged H_2 levels with a realistic seasonal cycle imposed. Depths where the H_2 concentration varied by more than 1% from the annual average were excluded from the reconstruction. The cut-off depths were 62 m, 66 m, and 50 m for NEEM, Summit and Tunu respectively. Unlike Greenland, Antarctic H_2

reconstructions are not sensitive to seasonality primarily because seasonal variability in atmospheric H_2 levels over Antarctica is less than half that of seasonal variability over Greenland.

4. Atmospheric reconstructions

285   Atmospheric H_2 reconstructions were carried out for each site independently (Figure 1). The NEEM, Summit, and Tunu sites have different physical characteristics (mean annual temperature and accumulation rate) and were sampled at different times. The firn air age distributions at NEEM and Summit are shown in Figure S1. The model inversions yield generally good agreement between the modeled and measured depth profiles for NEEM and Tunu (Figure 1b-d). Agreement is also good at Summit, except at the bottom of lock-in where the modeled depth profile increases monotonically with depth

290   while the deepest measurement shows a slight decrease.

      Firn air measurements from NEEM constrain atmospheric H_2 levels after 1950. The NEEM reconstruction shows atmospheric H_2 increasing from 1950-1989 at an average rate of 3.1 ppb y^{-1} (425-545 ppb). After 1989, atmospheric levels decrease at an average rate of 1.6 ppb y^{-1} reaching 515 ppb in 2008. Summit firn air is younger, yielding an atmospheric history beginning in 1975. The Summit reconstruction shows atmospheric H_2 increasing from 505-535 from 1975 to 1994, an average

295   rate of 1.5 ppb y^{-1}. After 1994 there is a slight decrease in atmospheric H_2 levels until 2003. After 2003, atmospheric H_2 decreases more rapidly at a rate of 1.5 ppb y^{-1}, reaching 515 ppb in 2013. Tunu firn air is considerably older, showing a rise in atmospheric H_2 from 370-510 ppb from 1930 to 1992, an average rate of 2.3 ppb y^{-1}. After 1992, H_2 levels decreased at a rate of 1.5 ppb y^{-1} to just over 500 ppb in 1996.

      All three reconstructions show H_2 levels rising during the mid-late 20th century with a maximum in atmospheric H_2

300   near 1990. The maximum is somewhat later and broader in the Summit reconstruction compared to the other two sites. There is only one measurement below the observed H_2 maximum at Summit, and that single measurement does not provide a sufficiently strong constraint on the reconstruction to generate the sharper maximum observed in the NEEM and Tunu reconstructions. We conducted another reconstruction using the Summit data with the uncertainty on the measurements reduced by 25%. Reducing the uncertainty on the Summit measurements imposes tighter constraints on the reconstruction and

305   forces better agreement between the modeled and measured depth profiles. This reconstruction shows an earlier maximum (1992) and a significantly more rapid rise in H_2 levels from 1975-1992, in better agreement with the reconstructions from NEEM and Tunu (Figure S2). The reconstructed decrease during the mid to late-1990's is still somewhat slower than in other two reconstructions.

      Although the trends observed in the NEEM and Tunu reconstructions are in good agreement, there is an offset of

310   roughly 35 ppb in absolute reconstructed H_2 levels (Figure 1a). We suspect that the offset is due to a calibration problem in the Tunu data. Those measurements were made in 1996, the same year that NOAA revised their H_2 working standard upward by 6.4%. Revising the Tunu measurements upward by 6.4% yields a reconstruction in near perfect agreement with the NEEM reconstruction. Furthermore, the probability model suggests that adjusting the Tunu measurements upwards by 7.1% yields

the best agreement between the three sites (see below), in good agreement with the 6.4% calibration adjustment. The original
315   NOAA laboratory notes for the Tunu samples indicate that the upward revision to the working standard was applied to the Tunu measurements but the data suggest that this revision was not actually applied. An alternative explanation for the offset between sites could be *in situ* H_2 production (see Section 8).

A "joint" reconstruction was carried out in which the most probable atmospheric history given the firn air data from all three sites is calculated (Figure 2). To account for the apparent offset between Tunu and the other sites, we introduced
320   another free parameter, γ , which is a dimensionless scalar multiplier for the data from Tunu. γ is drawn from a uniform prior between 0.9 and 1.1. Equation 9 is adapted for the measurements from Tunu.

$$\gamma \boldsymbol{h_{obs}} \sim N(\boldsymbol{Gm_{atm}}, \boldsymbol{\sigma}) \tag{10}$$

325   The posterior distribution for γ is approximately normally distributed around 1.071 with a standard deviation of 0.012, implying an offset of about 7.1% for the Tunu measurements. Atmospheric H_2 levels increase from 390 ppb in 1930 to 545 ppb in 1990 at an average rate of 2.6 ppb y^{-1}. After 1990, atmospheric H_2 starts to decrease at an average rate of 1.4 ppb y^{-1}, reaching 515 ppb in 2013. There is good agreement between the modeled and measured depth profiles for the joint reconstruction.

330

335

340

345

350

355

11

Figure 1: Atmospheric histories reconstructed independently from firn air profiles at three Greenland sites. a) purple line and shading- result from NEEM and associated ±1σ uncertainty; orange line and shading- result from Summit and associated ±1σ uncertainty; dark red line and shading- result from Tunu and associated ±1σ uncertainty black x's– annual mean synthetic Summit H₂ history (Section 5; Pétron et al., 2023; Langenfelds et al., 2002), purple crosses, orange triangles, and dark red squares- firn data plotted against modelled mean age for NEEM, Summit and Tunu respectively, the firn data have been adjusted for the effects of pore close-off fractionation; b) black markers-measured H₂ depth profile at NEEM; squares with error bars are measurements used in the reconstruction, and circles are measurements excluded from the reconstruction because of seasonality ; purple line and shading- modeled depth profile using the atmospheric history plotted in purple in a) with the propagated ±1σ uncertainty; the dashed black line indicates the top of lock-in zone c) and d) as in b) for Summit and Tunu respectively

370

12
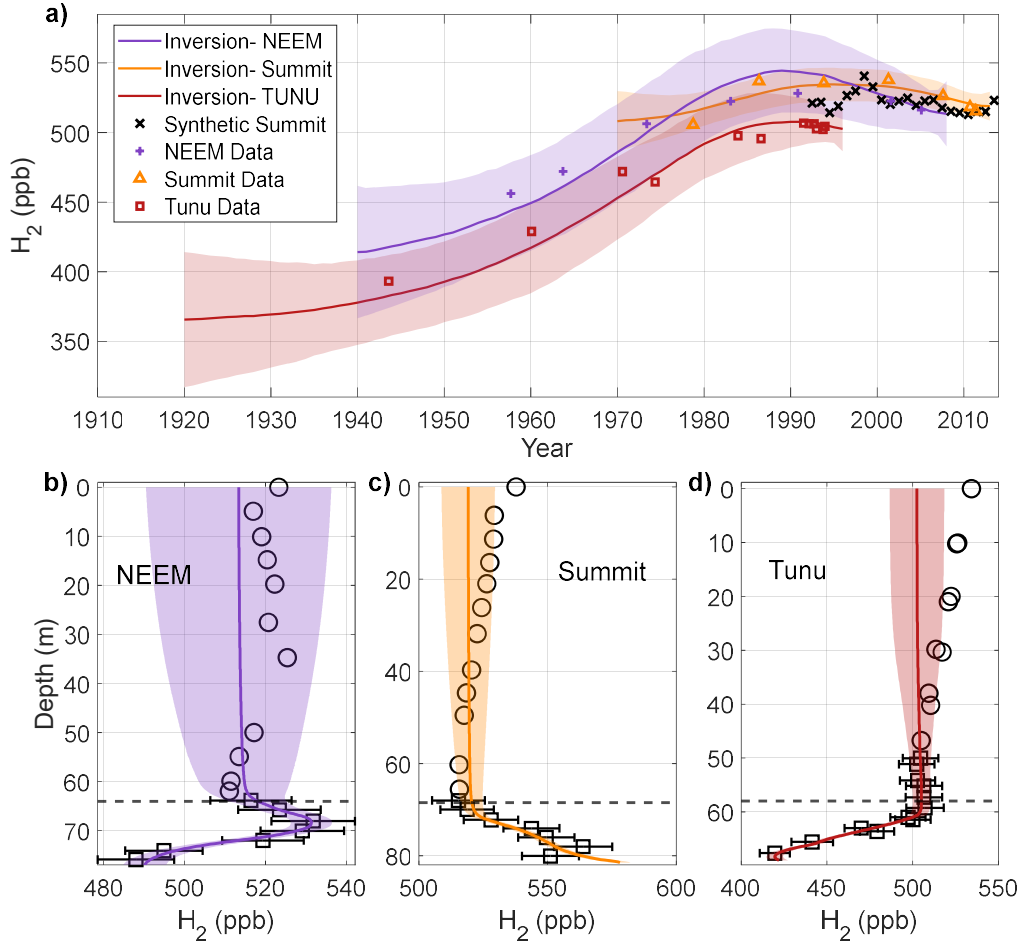
375 **Figure 2: Joint atmospheric H₂ reconstruction using firn air from three Greenland sites (NEEM, Summit, and Tunu). The reconstruction was conducted using equation 9 for NEEM and Summit, and equation 10 for Tunu (see text). All lines and markers are the same as in Figure 1. The Tunu measurements are adjusted upwards by 7.1% in panel a) and d) (see text).**
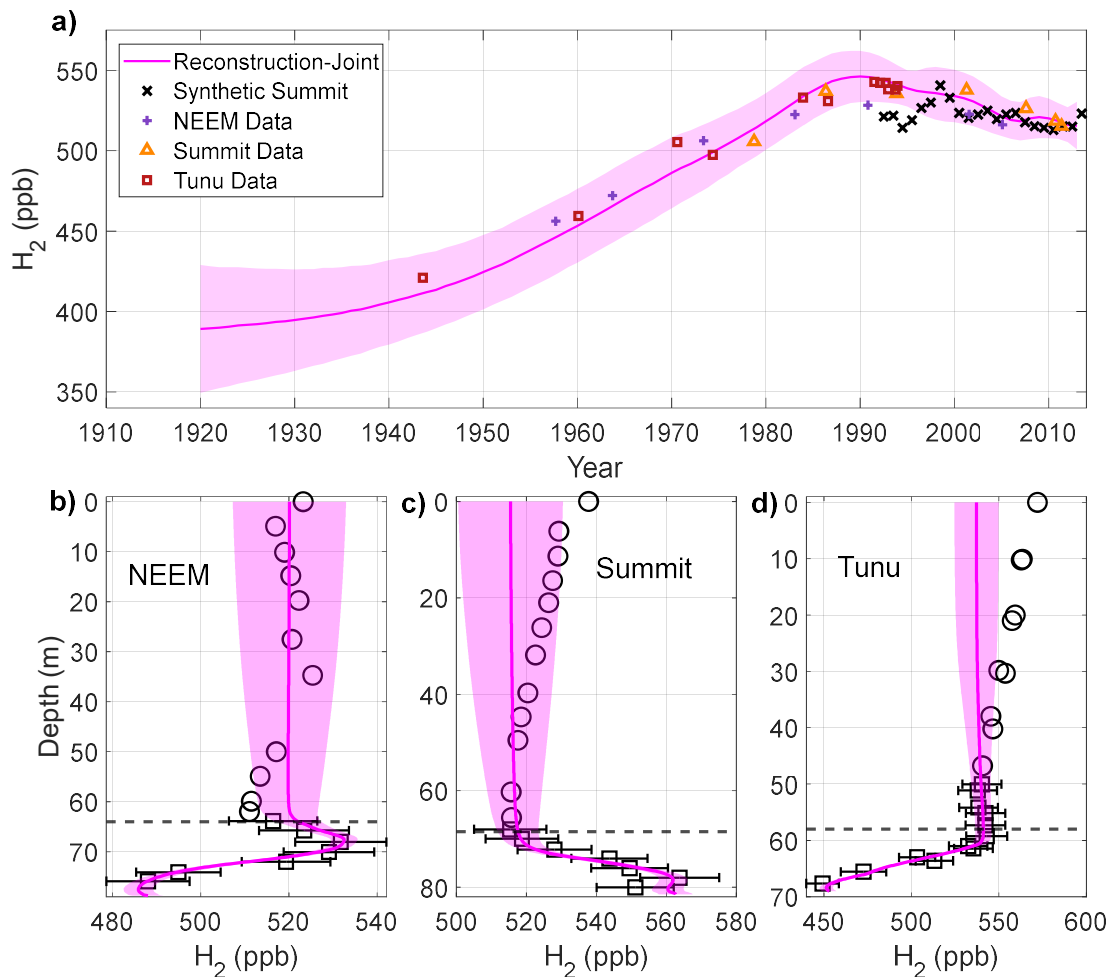
380

5. Comparison of firn air reconstruction with atmospheric flask measurements

The firn air reconstructions are compared to available atmospheric H₂ flask measurements from the high northern latitudes (Figure 3). Direct comparisons between the firn reconstructions and atmospheric measurements at other sites are complicated by spatial variability in H₂ levels in the high northern latitudes. The best temporal coverage for flask measurements is from the Barrow, Alaska and Alert, Nunavut sampling sites. Both sites sample the boundary layer and are influenced by their proximity to seasonally active soils. H₂ levels over Greenland are more representative of the free troposphere due to

13

higher elevation and remoteness from active soils. To make this comparison, we utilize NOAA/GML measurements at Alert, Nunavut and Summit, Greenland from 2010-present (revised to the MPI09 calibration scale; Pétron et al., 2023) and CSIRO measurements from Alert from 1992 onwards (also on the MPI09 scale).

During the 12 years of NOAA/GML measurements at Summit and Alert, the offset between Summit and Alert varies from a minimum of 18.9 ppb to a maximum of 29.4 ppb with a mean offset of 25.4 ppb ± 3.0 ppb (1σ) with Summit levels higher than Alert. We added this offset to the longer CSIRO Alert time series to generate a longer "synthetic Summit" flask history, assuming that the offset remains constant through time (Figures 1-4, 8). The most conspicuous feature of the synthetic Summit history is a sharp peak in H_2 levels during 1998 which can be attributed to increased biomass burning emissions during the strong 1997-1998 ENSO event (Langenfelds et al., 2002; van der Werf et al., 2004). Firn air cannot resolve such high frequency variability due to diffusive smoothing, so that feature is absent from our reconstructions. Excepting the 1998 peak, synthetic Summit H_2 levels are largely constant between 525 and 515 from 1992-2013. In contrast, the joint reconstruction shows a trend with H_2 levels decreasing from 545 to 515 ppb over the same time period.

We also examined the atmospheric data for evidence of the H_2 maximum around 1990 indicated by the firn air reconstruction. If this peak had occurred in the atmosphere, we would expect similar trends at all of the high latitude flask sites despite the differences in absolute H_2 levels. Here we examine flask measurements from Barrow, Alaska (Khalil & Rasmussen, 1990; NOAA/GML) and Alert, Canada (CSIRO; Figure 3). The measurements from NOAA/GML from 1992-2005 were corrected to the MPI09 calibration scale using the matched flask intercomparison project mentioned previously. The Khalil & Rasmussen (1990) data are reported on an independent calibration scale which has not been intercompared to the MPI09 calibration scale. The Barrow data from Khalil & Rasmussen (1990) shows an increase in atmospheric H_2 of 2.1 ppb y^{-1} from 1985-1989 and the subsequent NOAA/GML data show a decrease in atmospheric H_2 from 1989-1993, at a rate of 5.0 ppb y^{-1}. The reason for the rapid decrease in observed H_2 levels in the NOAA/GML data is not clear. At that time, anthropogenic emissions of H_2 were likely decreasing but not rapidly enough to account for the observed decrease (Hoesly et al., 2018; Paulot et al., 2021). It is possible that the observed decrease is linked to NOAA's drifting calibration scale as discussed in Section 2.2. Together, the trends in these two data sets imply a maximum in atmospheric H_2 in 1989, in agreement with the firn air reconstructions. The strength of this conclusion is questionable, because the flask intercomparison project did not include data prior to 1992. From 1993-2010, there is no discernible trend in atmospheric H_2 at either Barrow or Alert, while the firn air reconstructions show a slow decrease in atmospheric H_2. The flask measurements suggest a sharper maximum and more rapid stabilization than the firn air reconstructions.

Firn diffusion imposes smoothing on atmospheric reconstructions. To test whether the breadth of the atmospheric H_2 peak and slow subsequent decrease in the in the firn air reconstruction could be an artifact of that smoothing, we forced the firn air model with a synthetic atmospheric history. The synthetic history was identical to the joint reconstruction before 1989, decreasing by 5 ppb y^{-1} decrease from 1989- 1993 (as observed in the Barrow flask measurements) and subsequently decreases by 0.5 ppb y^{-1}, reaching the same atmospheric concentration as the joint reconstruction in 2013. The depth profiles generated by the model when forced with the synthetic history show poorer agreement with the measured firn H_2 than the levels generated

14

by the joint reconstruction (Figure S5). This result demonstrates that the firn air measurements are more consistent with a broad peak and slow decrease in H_2 levels than a sharp peak, rapid decrease, and stabilization.

425

Figure 3: Comparison of the joint Greenland firn air reconstruction with high northern latitude flask measurements. Magenta line and shading- joint reconstruction as in Figure 2a; purple lines- monthly (solid) and annually-averaged (dashed) flask measurements from Barrow, Alaska made by Khalil & Rasmussen (1990); Blue lines- monthly and annually-averaged flask measurement from Barrow, Alaska made by NOAA/GML (Novelli et al., 1999; Novelli, 2006);
430 **Red line- annual mean synthetic Summit H_2 history (Section 5; Pétron et al., 2023, Langenfelds et al., 2002); Yellow lines- monthly and annually-averaged flask measurement from Alert, Nunavut made by CSIRO (Langenfelds et al., 2002). Measurements from NOAA/GML were empirically corrected to the MPI09 calibration scale using a matched flask inter-comparison project between CSIRO and NOAA/GML.**
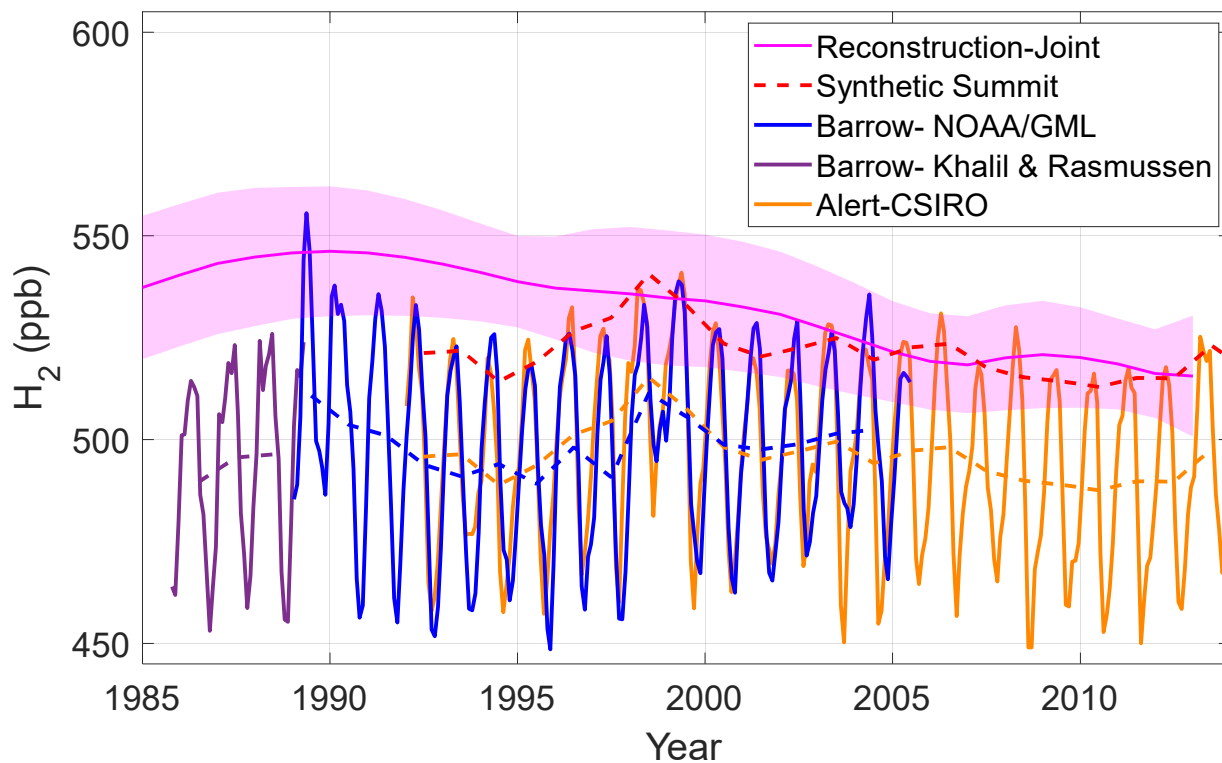
435

## 6. Comparison to previous firn air reconstructions

Petrenko et al. (2013) produced two atmospheric H_2 reconstructions from the NEEM firn air data. The reconstructions were generated using two different models: LGGE-GISPA and INSTAAR. Neither of those models include pore close-off fractionation, and Patterson et al. (2021) suggested that the maximum in atmospheric H_2 inferred from the NEEM firn air could be an artifact of ignoring pore close-off fractionation. Petrenko et al (2013) used the matrix inversion method of Rommelaere et al. (1997), which requires a prescribed smoothing parameter to fully constrain the inversion. Those results were corrected for a calibration revision (see Supplement) and are compared to our joint reconstruction (Figure 4a). The LGGE-GISPA reconstruction shows a rapid rise in H_2 levels from 1960-1990, and a rapid decrease from 1990-2008. The INSTAAR reconstruction shows H_2 levels rising more gradually from 1960-1985 and decreasing gradually thereafter. The rate of increase of H_2 levels prior to 1990 in our joint reconstruction falls between the rates of increase from the LGGE-GISPA and INSTAAR reconstructions. The timing of the atmospheric peak in our joint reconstruction shows good agreement with the timing from the LGGE-GISPA reconstruction, but the magnitude of the peak is in better agreement with the INSTAAR reconstruction. The rate of the decline in atmospheric H_2 from 1990-2008 from our joint reconstruction is nearly identical to the rate from the INSTAAR reconstruction. The late 20th century maximum in atmospheric H_2 is a robust feature of these Greenland firn air reconstructions. According to the UCI_2 model, pore close-off induced enrichment is <1% at the depth of the observed H_2 maximum in the lock-in zone. That is, the observed lock-in maximum is not caused by enrichment, but by a historical atmospheric maximum. However, there is evidence that the UCI_2 model underestimates the impacts of pore close-off fractionation at the Greenland sites. The implications of this underestimate for the atmospheric maximum are investigated and discussed in Section 7.

We conducted a similar joint reconstruction for H_2 firn measurements from two Antarctic sites: South Pole and Megadunes. The results of that joint reconstruction are compared to previously published reconstructions from those individual sites from (Patterson et al., 2020; 2021; Figure 4b). The differences between the joint reconstructions and the previously published reconstructions are relatively minor. The joint reconstruction shows a slightly slower increase in H_2 levels prior to 1965 and a more rapid increase from 1965-1980. After 1980, the joint reconstruction is in good agreement with the previously published reconstructions. Overall, the earlier Antarctic reconstructions exhibit a more uniform rate of increase over the past century. This is likely due to the use of an arbitrary smoothing parameter in the earlier studies, while an autocorrelation function was used in the joint reconstruction.

16

Figure 4: Comparison of our joint reconstructions with previously published firn air reconstructions a) Magenta line and shading, purple crosses, orange triangles, and dark red squares- joint Greenland reconstruction and firn air data as in Figure 2a; purple lines- Reconstructions from Petrenko et al. (2013) using the LGGE-GISPA model (dotted line) and INSTAAR model (dashed line); black x's- annual mean synthetic Summit H_2 history (Section 5; Pétron et al., 2023, Langenfelds et al., 2002). b) Blue line and shading- joint Antarctic reconstruction and associated $\pm1\sigma$ uncertainty; dashed maroon line- South Pole firn air reconstruction from Patterson et al., 2020; dashed red line- Megadunes firn air reconstruction from Patterson et al., 2021; black x's- H_2 annual means from measurements made by NOAA/GML at Palmer, Syowa, South Pole, and Halley Stations, Antarctica and Cape Grim Observatory, Tasmania (Novelli et al., 1999; Novelli, 2006); black circles- H_2 annual means from measurements made by CSIRO at Casey, South Pole, and Mawson Stations, Antarctica and Cape Grim and Macquarie Island, Tasmania (Langenfelds et al., 2002); H_2 annual means from measurements made by Khalil & Rasmussen (1990) at Palmer Station, Antarctica, and Cape Grim, Tasmania, purple squares and green triangles- firn air data plotted against modelled mean age for Megadunes and South Pole respectively, the data have been adjusted for pore close-off fractionation.
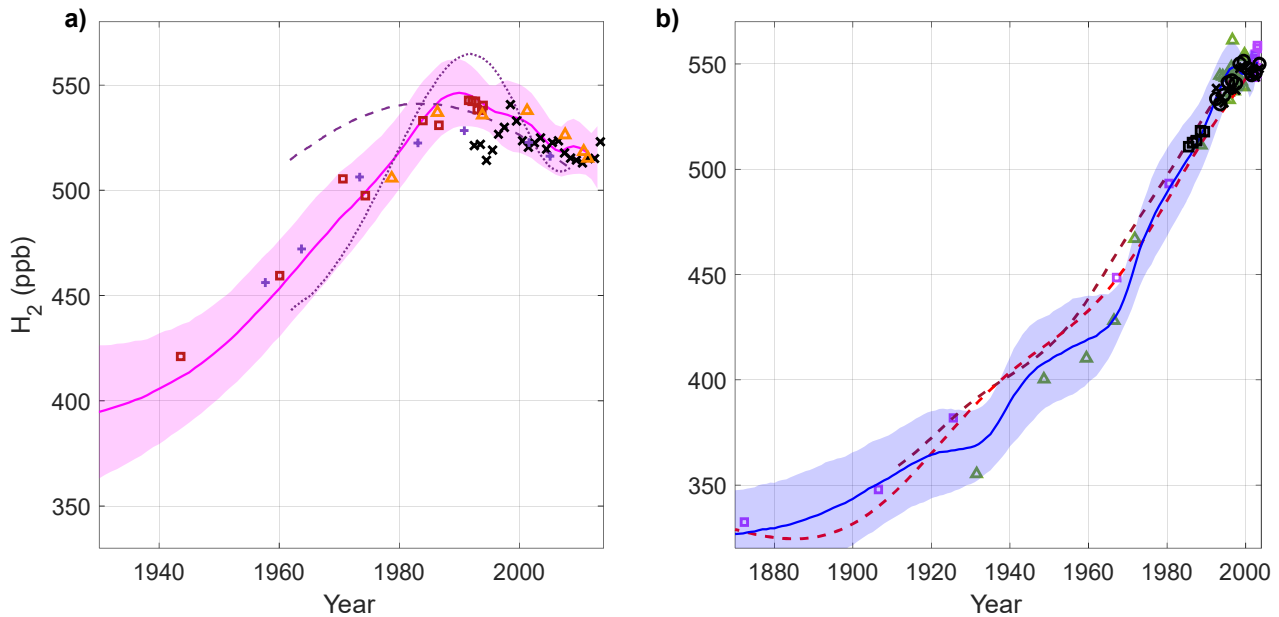
7. Investigating the impact of bias in the pore close-off fractionation parameterization

Ne and H_2 have similar permeability in ice due to their similar molecular diameters (Patterson & Saltzman, 2021; Satoh et al., 1996). Atmospheric Ne is constant, making it a useful tracer for assessing the effects of pore close-off fractionation. The UCI_2 firn air model underestimates pore close-off induced Ne enrichment at the base of the firn at NEEM and Summit. If a firn air model underestimates Ne enrichment, it is highly likely to also underestimate pore close-off enrichment for H_2. An underestimate of pore close-off induced enrichment would yield a reconstruction that is biased high, and a high bias could be responsible for the reconstructed 1990's peak in H_2 that is not observed in the surface air flask network measurements and for the differing trends in the reconstruction and the surface air flask network after the peak. Additionally, the bias could account for the unexpectedly high reconstructed Greenland H_2 levels relative to reconstructed Antarctic levels. We consider bias in the

Greenland record to be more likely than bias in the Antarctic record because there is good model-measurement agreement for Ne enrichment at the two Antarctic ice core sites (Figure S8). Additionally, the individual Antarctic reconstructions are in good agreement with each other and with high latitude Southern Hemisphere atmospheric flask measurements since the late 1980's (Figure 4b; Patterson et al., 2020; 2021).

Pore close-off fractionation is expected to substantially enrich H_2 and Ne levels in base of the firn (Section 3.1). $\delta^{22}Ne/N_2$ at the base of the firn was measured as 179‰ at NEEM and 112‰ at Summit where $\delta^{22}Ne/N_2$ of a sample is defined based on the relative mixing ratios of ^{22}Ne and N_2:

$$(\delta^{22}Ne/N_2)_{sample} = [(^{22}Ne/N_2)_{sample}/(^{22}Ne/N_2)_{atmospher} - 1] * 1000 \qquad (11)$$

The UCI_2 firn air model generates enrichments of only 122‰ at NEEM and 90‰ at Summit at the base of the firn, significantly lower than the measurements (Figure 5). The Ne content of the firn air at Tunu has not been measured. Because mixing between the closed bubbles and open pores affects the modeled H_2 age distributions, measurements cannot be empirically corrected for pore close-off fractionation as they are for gravitational fractionation (equation 2; Figure S7). Instead, pore close-off fractionation must be explicitly modeled.

At equilibrium, modelled pore close-off fractionation is controlled primarily by the ratio of the volume-weighted average pressure in the open and closed pores to the ambient pressure, adjusted for mixing. We introduce a new parameter, R:

$$R = (P_{bubble}s_c/s_{total} + P_{ambient}s_o/s_{total})/P_{ambient} \qquad (12)$$

In the UCI_2 model, R begins to increase too deep in the firn to capture the shallower $\delta^{22}Ne/N_2$ measurements (Figure 5; Figure 7). As a first attempt to improve agreement between measured and modeled Ne enrichment, we re-tuned the closed porosity profiles for NEEM and Summit to optimize model-measurement agreement for Ne enrichment using previously published parameterizations, including Schwander et al. (1989), Goujon et al. (2003), and Mitchell et al. (2015). However, in all cases, the optimization yielded closed porosity profiles that are qualitatively different from previously published estimates and probably unrealistic. When the optimizations were constrained to generate realistic closed porosity profiles, in all cases, we found that R increases too rapidly with depth to capture the $\delta^{22}Ne/N_2$ at both the top and the bottom of the lock-in zone. Therefore, in order to generate the necessary R profile while maintaining a realistic closed porosity profile, some other physical process must be modified in addition to the closed porosity profile. Possible candidates include the rate of densification, the rate of bubble close-off, and the rate of pressurization of bubbles. A detailed observation-based investigation of these processes at these sites would require field data that does not currently exist. Instead, we explored how altering the model parameterizations of these processes could improve the model-measurement agreement for Ne and examined the sensitivity of the firn air reconstruction to various physical assumptions.

18

Figure 5: Measured and modelled δ²²Ne/N₂ at NEEM (a) and Summit (b). Magenta lines- δ²²Ne/N₂ generated by the original UCI_2 model; dashed lavender lines- δ²²Ne/N₂ generated by the model with seasonal layering implemented (Section 7.1); maroon lines- δ²²Ne/N₂ generated by the model with reduced bubble compression (Section 7.2); dotted cyan lines- δ²²Ne/N₂ generated by the model with both seasonal layering and reduced bubble compression (Section 7.3); black squares- δ²²Ne/N₂ measurements corrected for gravitational fractionation and depth-averaged.
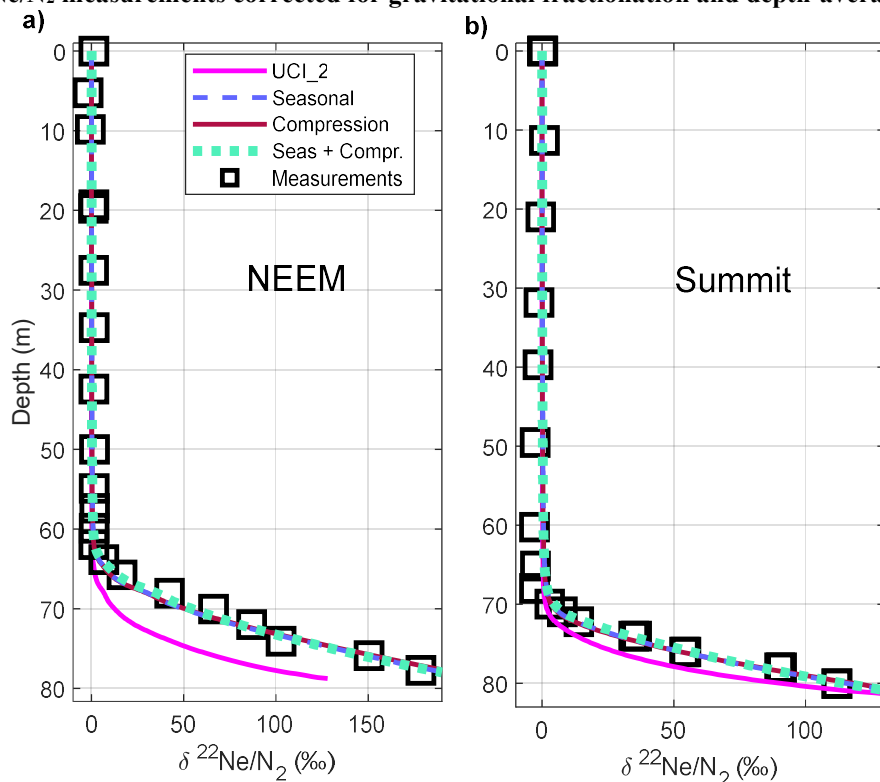
7.1 Method 1: Seasonal layering

Here we explored whether incorporating seasonal differences in densification could yield improved model-measurement agreement for Ne. Winter layers at both NEEM and Summit densify more rapidly than summer layers (Martinerie et al., 1992; Fujita et al., 2014). Fujita et al. (2014) attribute increased winter densification and deformation to seasonal differences in ion concentrations in the snow. Fujita et al. (2014) further show that bubbles occlude and pressurize preferentially in the dense winter layers before the summer layers. The UCI_2 model (and most firn air models) utilizes seasonally averaged bulk density and porosity to calculate bubble close-off and pressurization. This should lead to errors because of the non-linearities in the parameterization. The importance of layering in the firn to bubble trapping has been discussed extensively by Mitchell et al. (2015) and Fourteau et al. (2017).

In this experiment, we divide each model layer into a winter and summer "sub-layer." We arbitrarily specify that half of the mass of each layer is winter accumulation and half is summer accumulation. The density of each sub-layer is estimated based on Fujita et al., (2014; Figure S6), and the total porosity of the sub-layers is calculated using equation 1. The bulk density

19

of the firn is not changed from the original model. The original bulk closed porosity profile does not yield agreement between measured and modeled Ne enrichment, so the closed porosity profile is revised. The closed porosity of each sub layer (s_c) is prescribed as a function of the total porosity and density of that sub layer:

555
$$s_c = \frac{s_{total}}{1+\exp\left(-m(\rho_{firn}-\rho_0)\right)} \tag{13}$$

Where m and ρ_0 are free parameters that are tuned to yield agreement between measured and modeled Ne enrichment (Table 3; Figures 5 and 7). It has been demonstrated that winter and summer layers have similar close-off characteristics as a function of density, so the tuneable parameters are the same for both winter and summer sub-layers (Martinerie et al., 1992; Fourteau

560 et al. 2017). Bubble close-off and pressurization is calculated independently for winter and summer sub-layers using the same parameterization as in the UCI_2 model after Severinghaus & Battle (2006; equations A11-A13). Then, the bulk closed porosity and bubble pressure of each layer is determined from its constituent sub-layers, and the model is run as before using the calculated bulk properties. New H_2 age distributions are calculated, and the new age distributions are used to generate a revised joint reconstruction (Section 3.2; Figures 6 and 8).

565

7.2 Method 2: Reduced bubble compression

The bubble pressurization scheme used in the UCI_2 model assumes that closed bubbles compress at the same rate as the total porosity after Severinghaus & Battle (2006). Bubble trapping models that assume iso-compression have been shown to overestimate total air content in bubbles at the Lock-in and Vostok sites in East Antarctica (Fourteau et al., 2017). In that

570 work, better model-measurement agreement was achieved by reducing the compressibility of closed bubbles by 50%. Here, we explored whether reducing the compressibility of bubbles could yield improved model-measurement agreement for Ne enrichment. We modified equation A12 in Severinghaus & Battle (2006), which calculates the incremental new volume of air at ambient pressure ($\Delta V_{b(i)}$) occluded in bubbles between layer (i-1) and layer (i) per unit volume of firn:

575
$$\Delta V_{b(i)} = \frac{2\left\{s_{c(i)}-s_{c(i-1)}\left[(1-k_{comp})+k_{comp}\frac{s_{total(i)}}{s_{total(i-1)}}+\frac{\rho_{firn(i)}}{\rho_{firn(i-1)}}-1\right]\right\}}{(1-k_{comp})+k_{comp}\frac{s_{total(i)}}{s_{total(i-1)}}+1} \tag{14}$$

Where k_{comp} is a dimensionless free parameter that represents the degree of compressibility of the bubbles. In the limit of $k_{comp}=1$, equation 13 reduces to equation A12 of Severinghaus & Battle (2006), and bubbles compress at the same rate as the open pores. In the limit of $k_{comp}=0$, the bubbles are completely incompressible. Again, the original closed porosity profile does not

580 yield agreement with the measured Ne enrichment, so a new closed porosity profile is prescribed using equation 12. The three tuneable parameters from equations 12 and 13 (k_{comp}, $m,$ and ρ_0) are simultaneously optimized to give the best fit between

20

modeled and measured Ne enrichment (Table 3; Figures 5 and 7). Then, the model is used to calculate new age distributions for H_2, which are used for new reconstructions (Figures 6 and 8).

585   7.3 Method 3: Seasonal layering and reduced bubble compression

Lastly, we incorporated both seasonal layering and bubbles with reduced compressibility into the UCI_2 model. The density of the summer and winter layers is identical to Method 1. Instead of equation A12 from Severinghaus & Battle (2006), we use equation 13 to calculate bubble compression. Again, k_{comp}, m, and ρ_0 are tuned simultaneously to optimize the fit between measured and modeled Ne enrichment (Table 3; Figures 5 and 7). The model is run for H_2, and the new age
590   distributions are used to generate new H_2 reconstructions (Figures 6 and 8). We note that all three new parameterizations have a negligible effect on the modelling of trace gases like CO_2 and CH_4, which are not affected by pore close-off fractionation (Figure S9)

Table 3- Optimized tunable parameters for each method described in 7.1-7.3

| Site	Method 1			Method 2			Method 3		
	ρ_0 (kg m^{-3})	m (m^3 kg^{-1})	k_{comp}	ρ_0 (kg m^{-3})	m (m^3 kg^{-1})	k_{comp}	ρ_0 (kg m^{-3})	m (m^3 kg^{-1})	k_{comp}
NEEM	827	0.070	1.00	815	0.070	0.75	812	0.138	0.69
Summit	832	0.070	1.00	821	0.070	0.75	818	0.138	0.69

595

7.4 Revised reconstructions

The reconstructions generated by the three methods are very similar (Figure 8). The most significant consequence of increasing pore close-off fractionation is a reduction in the atmospheric maximum around 1990 and a more modest decrease
600   in atmospheric levels from 1990-2005. That is, higher modeled enrichment due to pore close-off fractionation yields correspondingly lower reconstructed H_2 levels. The 1990 maximum in the revised reconstruction is ~530 ppb, compared to 547 ppb in the original. After 1990, H_2 levels in the revised reconstructions decrease very slowly to 515 ppb in 2013, converging with the original reconstruction. The modest decrease in H_2 levels during the 1990's in the revised reconstructions is in better agreement with high northern latitude flask measurements and synthetic Summit history, which do not show a
605   discernible trend in atmospheric H_2 during the 1990's.

Because the older firn air that was sampled at Tunu is excluded from this analysis, the reconstructions are only meaningful after about 1950. Overall, H_2 levels in the revised reconstructions are reduced compared to the original reconstruction by 15-30 ppb from 1950-1990 (Figure 8). The new reconstructions remain 0-15 ppb higher than the Antarctic reconstructions, so the unexpectedly high reconstructed Greenland levels relative to Antarctic levels can be only partially
610   explained by the underestimate of pore close-off induced enrichment (Figure 9).

21

We can draw several important conclusions from these results: 1) H_2 atmospheric reconstructions are sensitive to pore close-off fractionation, 2) the large 1990's peak in the Greenland reconstructions is likely an artefact of underestimated pore close-off fractionation in the UCI_2 model, 3) as long as sufficient fractionation is achieved, the reconstructions are insensitive to the specific parameterization and internal model physics. All three of the approaches resulted in an increase in

615   the integrated area of the age distributions and a slightly older shift in mean age (Figure 6). All three methods greatly improve the fit between modelled and measured Ne enrichment at both sites. The similarity in optimized tuneable parameters suggest that a common mechanism underlies the UCI_2 model's underestimate of pore close-off induced enrichment at both NEEM and Summit (Table 3). It is likely that the common mechanism is associated with bubble close-off and pressurization. Further investigation of layering and bubble close-off using high resolution measurements of density, porosity, and air content, in

620   conjunction with measurements of highly diffusive trace gases like Ne or He would be useful in constraining pore close-off fractionation for future Greenland firn air work.

Figure 6: Open porosity H_2 age distributions resulting from several approaches to approximating pore close-off fractionation for H_2 at a depth of 75.9 m at NEEM (a) and at a depth of 80.1 m at Summit (b). Magenta lines- original

625   **UCI_2 model; dashed lavender lines, maroon lines, and dotted cyan lines are from the model with seasonal layering implemented (Section 7.1), with reduced bubble compression (Section 7.2), and with both seasonal layering and reduced bubble compression (Section 7.3) respectively.**
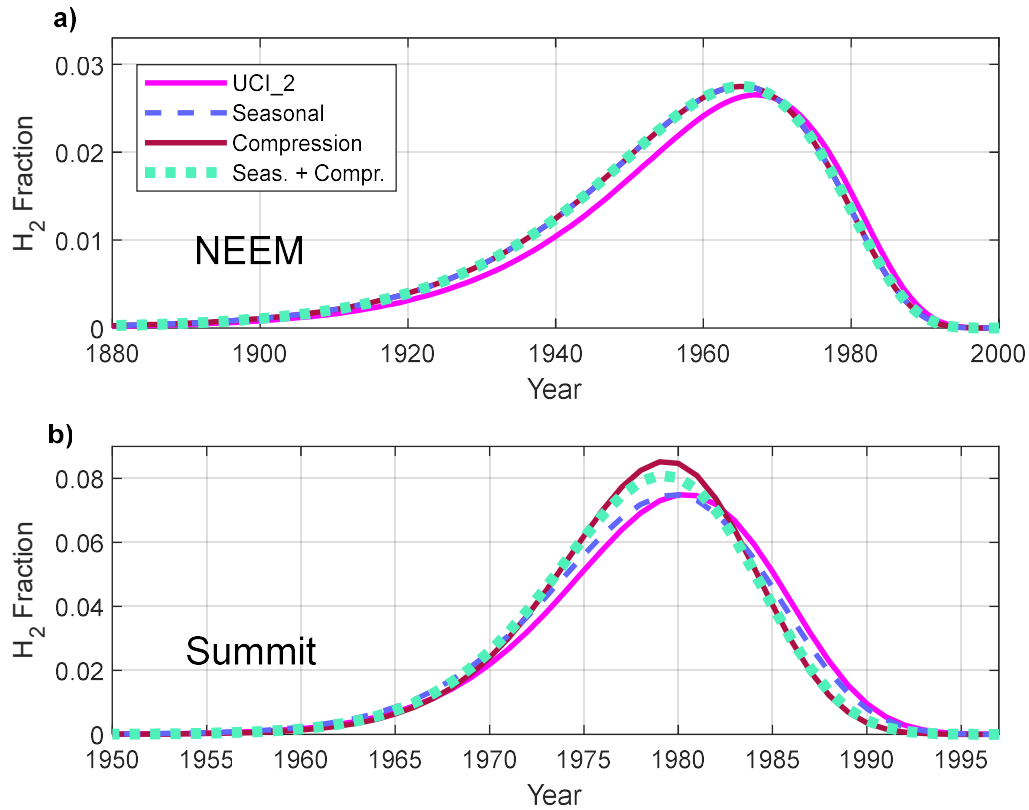
Figure 7: Model closed porosity fraction (i.e., s_c/s_{tot}) and R used for NEEM (a, b) and Summit (c, d). Magenta lines-original closed porosity fraction and R used in the UCI_2 model; dashed lavender lines, maroon lines, and dotted cyan lines are retuned closed porosity fraction and R used for the model with seasonal layering implemented (Section 7.1), with reduced bubble compression (Section 7.2), and with both seasonal layering and reduced bubble compression (Section 7.3) respectively.

635

640

23

645
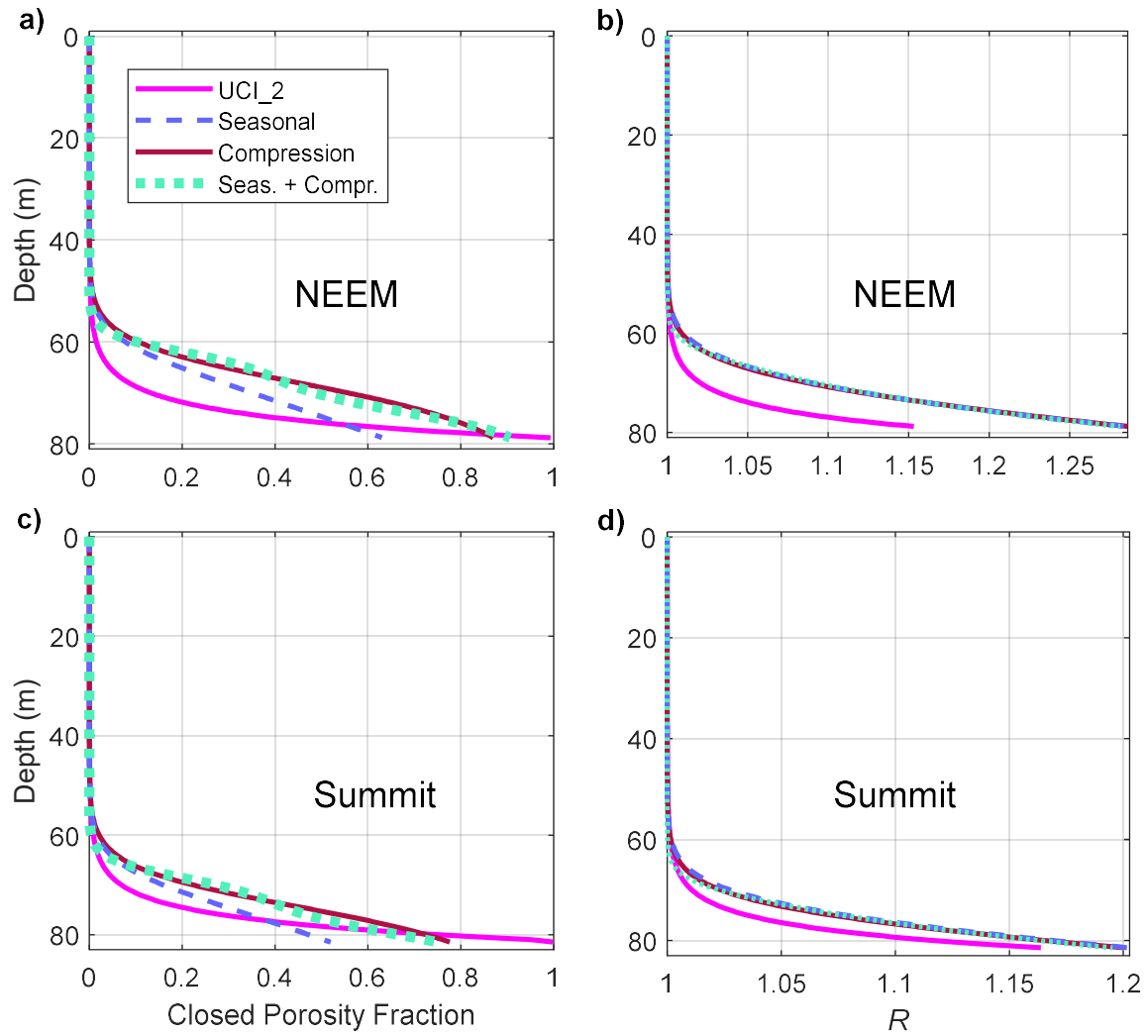
650

Figure 8: Reconstructions of atmospheric H$_2$ levels from Greenland firn air. Magenta line- joint reconstruction as in Figure 2a; dashed lavender lines, maroon lines, and dotted cyan lines are joint reconstructions calculated from the model with seasonal layering implemented (Section 7.1), with reduced bubble compression (Section 7.2), and with both seasonal layering and reduced bubble compression (Section 7.3) respectively; black x's annual mean synthetic Summit

655

H$_2$ history (Section 5; Pétron et al., 2023, Langenfelds et al., 2002). Grey shading is the approximate ±1σ uncertainty band for the three corrected reconstructions. The upper bound is the maximum of the sum of the three histories and their respective 1σ uncertainties for each year, and lower bound is the minimum of the difference between the three histories and their respective 1σ uncertainties.

660
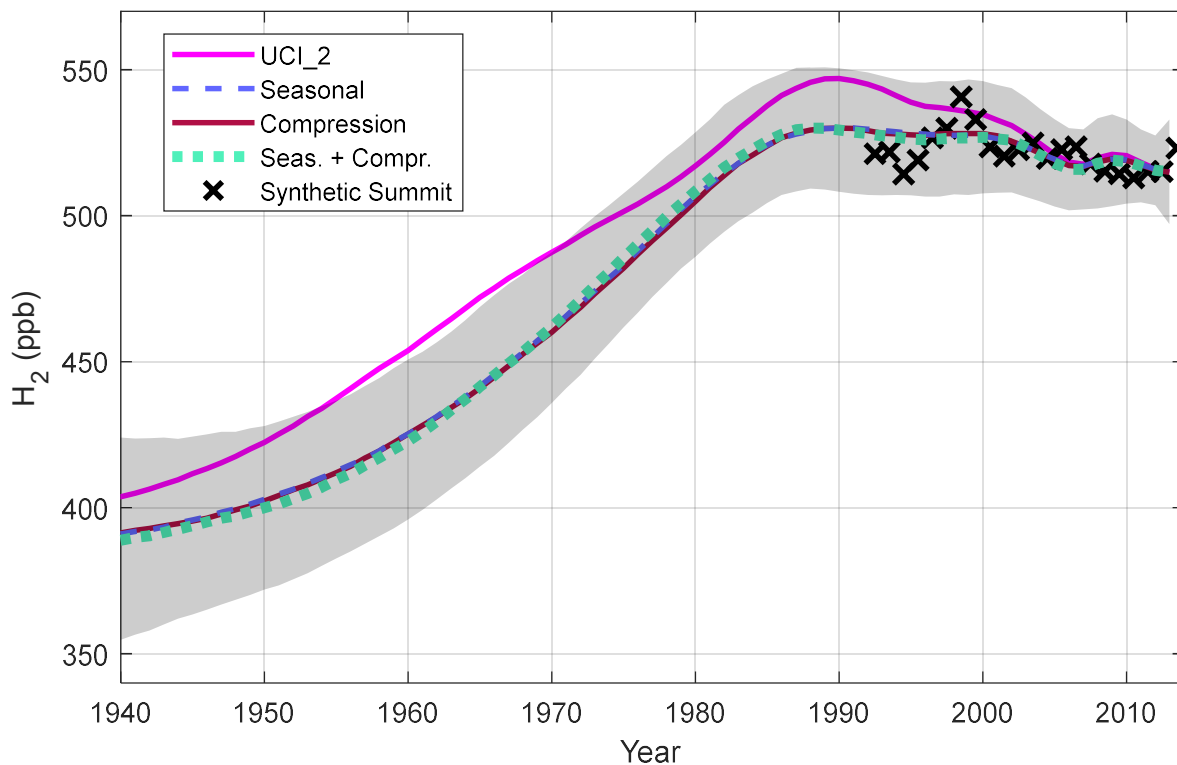
8. *In situ* production

665   It is possible that some of the differences between the independent reconstructions (Figure 1) could be caused by *in situ* production, but little is known about in situ H$_2$ production in snow and ice. It is useful to consider evidence for *in situ* production of CO because both trace gases may be photochemically produced from carbonyl-containing precursors. CO has

24

been shown to be produced photochemically from CH_2O in surface snow (Hahn et al., 2001). At Devon Island, Canada CO levels in the firn increased steadily with depth in both the diffusive and lock-in zones, exhibiting clear evidence of in situ production (Clark et al. 2007). By contrast, NEEM and Summit firn air both exhibit CO maxima in the firn air column associated with a late 20th century atmospheric maximum, with CO levels decreasing with increasing depth below (Petrenko et al., 2013). Petrenko et al. (2013) concluded in situ production at those sites was not sufficient to bias the atmospheric reconstruction. Those researchers used three lines of evidence to support their conclusion. First, the ice age at the depth of the observed lock-in zone CO peak is different at the two sites, so the peak cannot be attributed to a widely deposited layer of organic impurities. Second, the CO/CH_4 ratio at a given depth is in reasonable agreement at NEEM and Summit. CO and CH_4 have similar gas-phase diffusivities, so the mean age of the two gases at a given depth is comparable. CH_4 is known to be well preserved in Greenland firn air. If *in situ* production differentially affected CO levels at the two sites, it would be expected that CO/CH_4 ratios would diverge. Third, forcing a firn air model with an atmospheric flask derived CO history yields good agreement with the measured depth profile down to the top of lock-in zone where the firn air is too old to be constrained by flask measurements.

Greenland ice cores do exhibit evidence of in situ CO production. Early discrete measurements on Eurocore ice showed low, steady preindustrial CO levels (Hahn and Raynaud, 1998; Hahn et al., 1996). By contrast, Fain et al. (2022) reported higher and more variable CO levels from several Greenland sites (including NEEM and Tunu) using continuous flow and discrete methods. The elevated CO levels were apparently associated with localized organic impurities in the ice. The high variability in CO detected by the continuous flow method is not compatible with continuous production in the firn, where such signals should be smoothed by diffusion. It is therefore likely that the high frequency variability observed by Fain et al. (2022) originated below the lock-in zone. However, the ice core data do not preclude the possibility of some in situ production having occurred in the overlying firn.

The production of CO in Greenland firn air and ice is not well understood, and no physical mechanism has been proposed that can explain all of the observations. If the production is photochemical, one would expect it to be much faster in the firn than in ice, due to the much larger actinic flux. Until the mechanism is established, it is difficult to assess whether and to what extent *in situ* production might influence firn air H_2. Depending on the depth and mechanism, production of H_2 in the firn column would cause a high bias during some or all of our atmospheric reconstructions. Further research on this issue is needed.

9. Summary and conclusions

In this study we use all available firn air measurements of H_2 at Greenland and Antarctic sites to reconstruct atmospheric H_2 levels over the past century. The joint Antarctic reconstruction covers the 1900-2003 period and is based on firn air measurements from South Pole and Megadunes (Patterson et al., 2020; 2021). That reconstruction shows good site-to-site agreement and good agreement with the atmospheric flask network since the late 1980's. The good fit between measured

25

and simulated Ne enrichment obtained using the UCI_2 firn air model gives us high confidence in the modelling of pore close-off fractionation at the Antarctic sites.

Reconstructing H_2 levels over Greenland is more challenging because of inter-site biases and because the standard UCI_2 firn air model underestimates the enrichment of Ne at NEEM and Summit. It is likely that the model also underestimates
705　pore close-off induced enrichment of H_2 because of the similar permeability of the two gases in ice (Patterson & Saltzman, 2021; Satoh et al.1996). Three alternative parameterizations of pore close-off fractionation were explored to assess the sensitivity of the reconstructions to an underestimate of pore close-off induced enrichment. These revised reconstructions all show a less prominent atmospheric maximum and more stable H_2 levels during the late 20th century, in better agreement with the atmospheric flask measurements. Additionally, the alternative parameterizations of pore close-off fractionation yield better
710　model-measurement agreement for $\delta^{22}Ne/N_2$. The improved agreement indicates that the reconstructions generated by the alternative parameterizations is probably more realistic than the reconstruction generated by the UCI_2 model. We note that all of the alternative model versions do a an equally good job of reconstructing atmospheric histories of low permeability trace gases, such as CO_2 and CH_4 (Figure S9).

There is clearly uncertainty regarding the modelling of the physical processes influencing pore close-off fractionation,
715　particularly in Greenland firn air. A path to increasing confidence in firn air reconstructions for H_2 is to obtain new observations of firn air chemistry with high resolution measurements of firn density, porosity, and bubble total air content. Absent additional measurements, we believe that the results presented in Figure 9 are the best estimate for the evolution (and uncertainty) of atmospheric H_2 during the 20th century over Antarctica and Greenland. Ice core records at high accumulation sites should also be collected in order to constrain H_2 levels over the late pre-industrial and industrial eras. Such records will be important to
720　better understanding the global H_2 cycle, the impact of human activities on H_2 in the past, and the atmospheric response to increasing anthropogenic H_2 emissions in a warming climate.

One surprising result is that our reconstructions show higher H_2 levels over Greenland than over Antarctica prior to 1990. This implies a reversal in the sign of the interhemispheric difference during the late 20th century. It is believed that Northern hemispheric H_2 levels are lower than Southern hemisphere levels today due to strong uptake of atmospheric H_2 by
725　Northern hemisphere soils. The N/S interhemispheric difference in atmospheric H_2 occurs in spite of the fact that direct anthropogenic emissions of H_2 occur predominantly in the northern hemisphere. The dominance of northern hemispheric soil sink is largely a function of the asymmetry in land area between the two hemispheres. While the soil sink may vary over time due to changes in ecosystems, land use, or climate, a dramatic change would be required in order to have caused a reversal of the interhemispheric difference. In this respect, the firn air reconstructions present a challenge to our understanding of the
730　global atmospheric H_2 budget and careful examination of our conclusion that the northern hemisphere firn air reconstruction is not biased by *in situ* H_2 production in Greenland firn.

26

735 **Figure 9: Best estimates for the atmospheric history of H_2 in Greenland and Antarctica over the past century. Blue line- joint Antarctic firn air reconstruction as in Figure 4b; Green line- joint Greenland firn air reconstruction obtained from the mean of the three reconstructions using revised pore close-off parameterizations (Seasonal, Compression, and Seasonal+Compression; shown in Figure 8). Shaded areas are ±1σ uncertainties.**
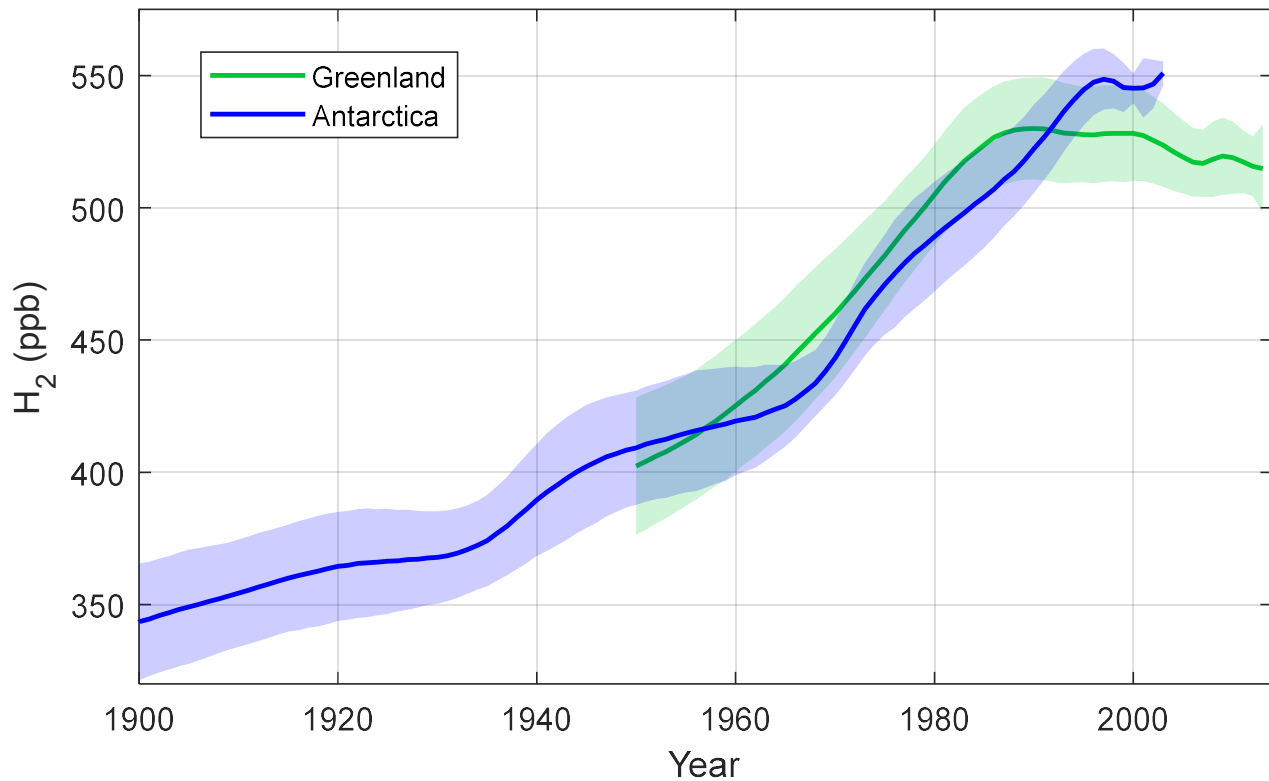
740 **Data and code availability**

The data and code used in this research has been submitted to the DRYAD data repository, and we will provide DOI identifiers before the end of the review process.

745 **Author contributions**

J.D.P. carried out the model simulations and data analysis; M.A. contributed to data analysis; A.M.C., G.P., R.L.L, and P.B.K. made calibration corrections and contributed atmospheric flask measurements; J.P.S. collected the field samples, measured $\delta^{22}Ne/N_2$, and assisted with firn air modeling; V.V.P collected field samples and contributed to firn air measurements, E.S.S. contributed to modeling, data analysis, and editing the manuscript; and J.D.P. wrote the manuscript.

750

Competing interests

The authors declare that they have no conflict of interest.

27

References

Aydin, M., Britten, G. L., Montzka, S. A., Buizert, C., Primeau, F., Petrenko, V., Battle, M. B., Nicewonger, M. R.,
760   Patterson, J., Hmiel, B., & Saltzman, E. S. (2020). Anthropogenic Impacts on Atmospheric Carbonyl Sulfide Since the 19th Century Inferred From Polar Firn Air and Ice Core Measurements. *Journal of Geophysical Research: Atmospheres*, *125*(16), 1–23. https://doi.org/10.1029/2020JD033074

Bader, H. (1964). Density of Ice as a Function of Temperature and Stress. *Special Report (U.S. Army Cold Regions Research and Engineering Laboratory)*, *64*, 1–6.

765 Battle, M., Bender, M., Sowers, T., Tans, P. P., Butler, J. H., Elkins, J. W., Ellis, J. T., Conway, T., Zhang, N., Lang, P., & Clarke, A. D. (1996). Atmospheric gas concentrations over the past century measured in air from firn at the South Pole. *Nature*, *383*(6597), 231–235. https://doi.org/10.1038/383231a0

Buizert, C., & Severinghaus, J. P. (2016). Dispersion in deep polar firn driven by synoptic-scale surface pressure variability. Cryosphere, 10(5), 2099–2111. https://doi.org/10.5194/tc-10-2099-2016

770 Buizert, C. (2013). Studies of firn air. In S. A. Elias & C. J. Mock (Eds.), *Encyclopedia of Quaternary Science 2* (pp. 361–372). Elsevier.

Buizert, C., Martinerie, P., Petrenko, V. v., Severinghaus, J. P., Trudinger, C. M., Witrant, E., Rosen, J. L., Orsi, A. J., Rubino, M., Etheridge, D. M., Steele, L. P., Hogan, C., Laube, J. C., Sturges, W. T., Levchenko, V. A., Smith, A. M.,
775   Levin, I., Conway, T. J., Dlugokencky, E. J., … Blunier, T. (2012). Gas transport in firn: Multiple-tracer characterisation and model intercomparison for NEEM, Northern Greenland. *Atmospheric Chemistry and Physics*, *12*(9), 4259–4277. https://doi.org/10.5194/acp-12-4259-2012

Butler, J. H., Battle, M., Bender, M. L., Montzka, S. A., Clarke, A. D., Saltzman, E. S., Sucher, C. M., Severinghaus, J. P., & Elkins, J. W. (1999). A record of atmospheric halocarbons during the twentieth century from polar firn air. *Nature*,
780   *399*(6738), 749–755. https://doi.org/10.1038/21586

Carpenter, B., Gelman, A., Hoffman, M. D., Lee, D., Goodrich, B., Betancourt, M., Brubaker, M. A., Guo, J., Li, P., & Riddell, A. (2017). Stan: A probabilistic programming language. *Journal of Statistical Software*, *76*(1). https://doi.org/10.18637/jss.v076.i01

Clark, I. D., Henderson, L., Chappellaz, J., Fisher, D., Koerner, R., Worthy, D. E. J., Kotzer, T., Norman, A. L., & Barnola,
785   J. M. (2007). CO2 isotopes as tracers of firn air diffusion and age in an Arctic ice cap with summer melting, Devon Island, Canada. *Journal of Geophysical Research Atmospheres*, *112*(1). https://doi.org/10.1029/2006JD007471

Derwent, R. G., Stevenson, D. S., Utembe, S. R., Jenkin, M. E., Khan, A. H., & Shallcross, D. E. (2020). Global modelling studies of hydrogen and its isotopomers using STOCHEM-CRI: Likely radiative forcing consequences of a future hydrogen economy. *International Journal of Hydrogen Energy*, *45*(15), 9211–9221.
790   https://doi.org/10.1016/j.ijhydene.2020.01.125

Dlugokencky, E., & Lan, X. (2020a). *Atmospheric Carbon Dioxide Dry Air Mole Fractions from the NOAA GML Carbon Cycle Cooperative Global Air Sampling Network, 1968-2019*. NOAA/ESRL. ftp://aftp.cmdl.noaa.gov/data/trace_gases/co2/

795 Dlugokencky, E., & Lan, X. (2020b). *Atmospheric Methane Dry Air Mole Fractions from the NOAA GML Carbon Cycle Cooperative Global Air Sampling Network, 1983-2019*. NOAA/ESRL. ftp://aftp.cmdl.noaa.gov/data/trace_gases/ch4/

Ehhalt, D. H., & Rohrer, F. (2009). The tropospheric cycle of H2: A critical review. *Tellus, Series B: Chemical and Physical Meteorology*, *61*(3), 500–535. https://doi.org/10.1111/j.1600-0889.2009.00416.x

Etheridge, D. M., Steele, L. P., Francey, R. J., & Langenfelds, R. L. (1998). Atmospheric methane between 1000 A . D . and present : Evidence of anthropogenic emissions and climatic variability. *Journal of Geophysical Research*, *103*(D13),
800 15979–15993.

Etheridge, D. M., Steele, L. P., Langenfelds, R. L., & Francey, R. J. (1996). Natural and anthropogenic changes in atmospheric CO2 over the last 1000 years from air in Antarctic ice and firn. *Journal of Geophysical Research*, *101*(D2), 4115–4128. https://doi.org/10.1074/jbc.271.44.27509

805 Faïn, X., Rhodes, R. H., Place, P., Petrenko, V. V., Fourteau, K., Chellman, N., Crosier, E., McConnell, J. R., Brook, E. J., Blunier, T., Legrand, M., & Chappellaz, J. (2022). Northern Hemisphere atmospheric history of carbon monoxide since preindustrial times reconstructed from multiple Greenland ice cores. *Climate of the Past*, *18*(3), 631–647. https://doi.org/10.5194/cp-18-631-2022

Fourteau, K., Faïn, X., Martinerie, P., Landais, A., Ekaykin, A., Lipenkov, V., & Chappellaz, J. (2017). Analytical
810 constraints on layered gas trapping and smoothing of atmospheric variability in ice under low-accumulation conditions. *Climate of the Past*, *13*(12), 1815–1830. https://doi.org/10.5194/cp-13-1815-2017

Fujita, S., Hirabayashi, M., Goto-Azuma, K., Dallmayr, R., Satow, K., Zheng, J., & Dahl-Jensen, D. (2014). Densification of layered firn of the ice sheet at NEEM, Greenland. *Journal of Glaciology*, *60*(223), 905–921. https://doi.org/10.3189/2014JoG14J006

815 Fuller, E. N., Schettler, P. D., & Giddings, J. C. (1966). New method for prediction of binary gas-phase diffusion coefficients. *Journal of Industrial and Engineering Chemistry*, *58*, 18–27.

Goujon, C., Barnola, J. M., & Ritz, C. (2003). Modelling the densification of polar firn including heat diffusion: Application to close-off characteristics and gas isotopic fractionation for Antarctica and Greenland sites. *Journal of Geophysical Research D: Atmospheres*, *108*(24). https://doi.org/10.1029/2002jd003319

820 Haan, D., Martinerie, P., & Raynaud, D. (1996). Ice core data of atmospheric carbon monoxide over Antarctica and Greenland during the last 200 years. *Geophysical Research Letters*, *23*(17), 2235–2238. https://doi.org/10.1029/96GL02137

Haan, D., & Raynaud, D. (1998). Ice core record of CO variations during the last two millennia: atmospheric implications and chemical interactions within the Greenland ice. *Tellus B: Chemical and Physical Meteorology*, *50*(3), 253.
825 https://doi.org/10.3402/tellusb.v50i3.16101

Haan, D., Zuo, Y., Gros, V., & Brenninkmeijer, C. A. M. (2001). Photochemical Production of Carbon Monoxide in Snow. In *Journal of Atmospheric Chemistry* (Vol. 40).

Hmiel, B., Petrenko, V. v., Dyonisius, M. N., Buizert, C., Smith, A. M., Place, P. F., Harth, C., Beaudette, R., Hua, Q., Yang, B., Vimont, I., Michel, S. E., Severinghaus, J. P., Etheridge, D., Bromley, T., Schmitt, J., Faïn, X., Weiss, R. F., & Dlugokencky, E. (2020). Preindustrial 14CH4 indicates greater anthropogenic fossil CH4 emissions. *Nature*, *578*(7795), 409–412. https://doi.org/10.1038/s41586-020-1991-8

Hoesly, R. M., Smith, S. J., Feng, L., Klimont, Z., Janssens-Maenhout, G., Pitkanen, T., Seibert, J. J., Vu, L., Andres, R. J., Bolt, R. M., Bond, T. C., Dawidowski, L., Kholod, N., Kurokawa, J. I., Li, M., Liu, L., Lu, Z., Moura, M. C. P., O'Rourke, P. R., & Zhang, Q. (2018). Historical (1750-2014) anthropogenic emissions of reactive gases and aerosols from the Community Emissions Data System (CEDS). Geoscientific Model Development, 11(1), 369–408. https://doi.org/10.5194/gmd-11-369-2018

Jordan, A., & Steinberg, B. (2011). Calibration of atmospheric hydrogen measurements. *Atmospheric Measurement Techniques*, *4*(3), 509–521. https://doi.org/10.5194/amt-4-509-2011

Khalil, M. A. K., & Rasmussen, R. A. (1990). Global increase of atmospheric molecular hydrogen. *Nature*, *347*, 743–745. https://doi.org/10.1016/0021-9797(80)90501-9

Langenfelds, R. L., Francey, R. J., Pak, B. C., Steele, L. P., Lloyd, J., Trudinger, C. M., & Allison, C. E. (2002). Interannual growth rate variations of atmospheric CO2 and its δ13C, H2, CH4, and CO between 1992 and 1999 linked to biomass burning. *Global Biogeochemical Cycles*, *16*(3). https://doi.org/10.1029/2001gb001466

Martinerie, P., Raynaud, D., Etheridge, D. M., Barnola, J.-M., & Mazaudier, D. (1992). Physical and climatic parameters which influence the air content in polar ice. In *Earth and Planetary Science Letters* (Vol. 112).

Mitchell, L. E., Buizert, C., Brook, E. J., Breton, D. J., Fegyveresi, J., Baggenstos, D., Orsi, A., Severinghaus, J., Alley, R. B., Albert, M., Rhodes, R. H., McConnell, J. R., Sigl, M., Maselli, O., Gregory, S., & Ahn, J. (2015). Observing and modeling the influence of layering on bubble trapping in polar firn. *Journal of Geophysical Research*, *120*(6), 2558–2574. https://doi.org/10.1002/2014JD022766

Novelli, P. C. (2006). *Atmospheric Hydrogen Mixing Ratios from the NOAA GMD Carbon Cycle Cooperative Global Air Sampling Network, 1988-2005*. NOAA/ESRL.

Novelli, P. C., Crotwell, A. M., & Hall, B. D. (2009). Application of gas chromatography with a pulsed discharge helium ionization detector for measurements of molecular hydrogen in the atmosphere. *Environmental Science and Technology*. https://doi.org/10.1021/es803180g

Novelli, P. C., Lang, P. M., Masarie, K. A., Hurst, D. F., Myers, R., & Elkins, J. W. (1999). Molecular hydrogen in the troposphere: Global distribution and budget. *Journal of Geophysical Research*, *104*(D23), 30427–30444.

Patterson, J. D., Aydin, M., Crotwell, A. M., Pétron, G., Severinghaus, J. P., Krummel, P. B., Langenfelds, R. L. & Saltzman, E. S. (2021). H2 in Antarctic firn air: Atmospheric reconstructions and implications for anthropogenic emissions. *Proceedings of the National Academy of Sciences of the United States of America*, *118*. https://doi.org/10.1073/pnas.2103335118/-/DCSupplemental.90

Patterson, J. D., Aydin, M., Crotwell, A. M., Petron, G., Severinghaus, J. P., & Saltzman, E. S. (2020). Atmospheric History of H2 Over the Past Century Reconstructed From South Pole Firn Air. *Geophysical Research Letters*, *47*(14), 1–8. https://doi.org/10.1029/2020GL087787

Patterson, J. D., & Saltzman, E. S. (2021). Diffusivity and solubility of H2 in ice Ih: Implications for the behavior of H2 in polar ice. *Journal of Geophysical Research Atmospheres*, *126*, 1–14. https://doi.org/10.1029/2020JD033840

30

Paulot, F., Paynter, D., Naik, V., Malyshev, S., Menzel, R., & Horowitz, L. W. (2021). Global modeling of hydrogen using GFDL-AM4.1: Sensitivity of soil removal and radiative forcing. *International Journal of Hydrogen Energy*, *46*(24), 13446–13460. https://doi.org/10.1016/j.ijhydene.2021.01.088

870 Petrenko, V. v., Martinerie, P., Novelli, P., Etheridge, D. M., Levin, I., Wang, Z., Blunier, T., Chappellaz, J., Kaiser, J., Lang, P., Steele, L. P., Hammer, S., Mak, J., Langenfelds, R. L., Schwander, J., Severinghaus, J. P., Witrant, E., Petron, G., Battle, M. O., … White, J. W. C. (2013). A 60 yr record of atmospheric carbon monoxide reconstructed from Greenland firn air. *Atmospheric Chemistry and Physics*, *13*(15), 7567–7585. https://doi.org/10.5194/acp-13-7567-2013

875 Pétron, G., Crotwell, A., Kitzis, M., Madronich, D., Mefford, T., Moglia, E., Mund, J., Neff, D., Thoning, K., & Wolter, S. (2023). *Atmospheric Hydrogen Dry Air Mole Fractions from the NOAA GML Carbon Cycle Cooperative Global Air Sampling Network, 2009-Present [Data set]*. https://doi.org/10.15138/WP0W-EZ08

Pieterse, G., Krol, M. C., Batenburg, A. M., M. Brenninkmeijer, C. A., Popa, M. E., O'Doherty, S., Grant, A., Steele, L. P., Krummel, P. B., Langenfelds, R. L., Wang, H. J., Vermeulen, A. T., Schmidt, M., Yver, C., Jordan, A., Engel, A., 880 Fisher, R. E., Lowry, D., Nisbet, E. G., … Röckmann, T. (2013). Reassessing the variability in atmospheric H 2 using the two-way nested TM5 model . *Journal of Geophysical Research: Atmospheres*, *118*(9), 3764–3780. https://doi.org/10.1002/jgrd.50204

Pieterse, G., Krol, M. C., Batenburg, A. M., Steele, L. P., Krummel, P. B., Langenfelds, R. L., & Röckmann, T. (2011). Global modelling of H2 mixing ratios and isotopic compositions with the TM5 model. *Atmospheric Chemistry and* 885 *Physics*, *11*(14), 7001–7026. https://doi.org/10.5194/acp-11-7001-2011

Prather, M. J. (2003). An environmental experiment with H2. *Science*, *302*(5645), 581–582. https://doi.org/10.1126/science.1091060

Prinn, R. G., Weiss, R. F., Aduini, J., Arnold, T., Dewitt, H., Fraser, P. J., Ganesan, A. L., Gasore, J., Harth, C. M., Hermansen, O., Kim, J., Krummel, P. B., Li, S., Loh, Z. M., Lunder, C. R., Maione, M., Manning, A. J., Miller, B. R., 890 Mitreveski, B., … Zhou, L. (2019). *History of chemically and radiatively important atmospheric gases from the Advanced Global Atmospheric Gases Experiment (AGAGE)*. Carbon Dioxide Information Analysis Center (CDIAC), Oak Ridge National Laboratory (ORNL), Oak Ridge, (United States). https://doi.org/https://doi.org/10.3334/CDIAC/atg.db1001

Reid, R. C., Prausnitz, J. M., Sherwood, T. K., & Poling, B. E. (1987). *The properties of gases and liquids* (4th ed.). 895 McGraw-Hill.

Rommelaere, V., Arnaud, L., & Barnola, J. (1997). Reconstructing recent atmospheric trace gas concentrations from polar firn and bubbly ice data by inverse methods. *Journal of Geophysical Research*, *102*(D25), 30069–30083.

Satoh, K., Uchida, T., Hondoh, T., & Mae, S. (1996). Diffusion coefficient and solubility measurements of noble gases in ice crystals. *Proc, NIPR Symp.Polar Meteorol, G]Aciol*, *10*, 73–81.

900 Schwander, J., Barnola, J. M., Andrie, C., Leuenberger, M., Ludin, A., Raynaud, D., & Stauffer, B. (1993). The Age of the Air in the Firn and the Ice at Summit, Greenland. *Journal of Geophysical Research*, *98*, 2831–2838.

Schwander, J., Oeschger, H., & Langway, C. C. (1989). *The Environmental Record in Glaciers and Ice Sheets*. John Wiley.

Severinghaus, J. P., Albert, M. R., Courville, Z. R., Fahnestock, M. A., Kawamura, K., Montzka, S. A., Mühle, J., Scambos, T. A., Shields, E., Shuman, C. A., Suwa, M., Tans, P., & Weiss, R. F. (2010). Deep air convection in the firn at a

905   zero-accumulation site, central Antarctica. *Earth and Planetary Science Letters*, *293*(3–4), 359–367. https://doi.org/10.1016/j.epsl.2010.03.003

Severinghaus, J. P., & Battle, M. O. (2006). Fractionation of gases in polar ice during bubble close-off: New constraints from firn air Ne, Kr and Xe observations. *Earth and Planetary Science Letters*. https://doi.org/10.1016/j.epsl.2006.01.032

910 Severinghaus, J. P., Grachev, A., & Battle, M. (2001). Thermal fractionation of air in polar firn by seasonal temperature gradients. *Geochemistry Geophysics Geosystems*, *2*(7).

Solomon, S., Rosenlof, K. H., Portmann, R. W., Daniel, J. S., Davis, S. M., Sanford, T. J., & Plattner, G.-K. (2010). Contributions of Stratospheric Water Vapor to Decadal Changes in the Rate of Global Warming. *Science*, *327*(5970), 1219–1223. https//doi.org/10.1126/science.1182488

915 Trudinger, C. M., Enting, I. G., Etheridge, D. M., Francey, R. J., Levchenko, V. A., Steele, L. P., Raynaud, D., & Arnaud, L. (1997). Modeling air movement and bubble trapping in firn. *Journal of Geophysical Research Atmospheres*. https://doi.org/10.1029/96JD03382

van der Werf, G. R., Randerson, J. T., James Collatz, † G, Giglio, L., Kasibhatla, P. S., Arellano, A. F., Olsen, S. C., & Kasischke, E. S. (2004). Continental-Scale Partitioning of Fire Emissions During the 1997 to 2001 El Niño/La Niña
920   Period. Science, 303, 73–76. https://www.science.org

Wang, D., Jia, W., Olsen, S. C., Wuebbles, D. J., Dubey, M. K., Rockett, A. A., & Wuebbles, C. D. J. (2013a). Impact of a future H 2 -based road transportation sector on the composition and chemistry of the atmosphere – Part 1 : Tropospheric composition and air quality. *Atmospheric Chemistry and Physics*, *13*(2), 6117–6137. https://doi.org/10.5194/acp-13-6117-2013

925 Wang, D., Jia, W., Olsen, S. C., Wuebbles, D. J., Dubey, M. K., Rockett, A. A., & Wuebbles, C. D. J. (2013b). Impact of a future H 2 -based road transportation sector on the composition and chemistry of the atmosphere – Part 2 : Stratospheric ozone. *Atmospheric Chemistry and Physics*, *13*, 6139–6150. https://doi.org/10.5194/acp-13-6139-2013

Warwick, N., Griffiths, P., Keeble, J., Archibald, A., & Pyle, J. (2022). *Atmospheric implications of increased Hydrogen use*. https://www.gov.uk/government/publications/atmospheric-implications-of-increased-hydrogen-use